Self-Assembled Carbon Superstructures Achieving Ultra-Stable and Fast Proton-Coupled Charge Storage Kinetics

Ziyang Song, Ling Miao, Laurent Ruhlmann, Yaokang Lu, Dazhang Zhu, Liangchun Li, Lihua Gan, Mingxian Liu

Self-Assembled Carbon Superstructures Achieving Ultra-Stable and Fast Proton-Coupled Charge Storage Kinetics

Ziyang Song, Ling Miao, Laurent Ruhlmann, Yaokang Lv, Dazhang Zhu, Liangchun Li, Lihua Gan, and Mingxian Liu*

Ziyang Song, Dr. Ling Miao, Prof. Dazhang Zhu, Prof. Liangchun Li, Prof. Lihua Gan, Prof. Mingxian Liu
Shanghai Key Lab of Chemical Assessment and Sustainability, School of Chemical Science and Engineering, Tongji University, Shanghai 200092, P. R. China.
E-mail: liumx@tongji.edu.cn
Prof. Laurent Ruhlmann, Dr. Yaokang Lv
Institut de Chimie (UMR au CNRS n°7177), Université de Strasbourg, 4, rue Blaise Pascal CS 90032, F-67081 Strasbourg Cedex, France.
Dr. Yaokang Lv
College of Chemical Engineering, Zhejiang University of Technology, Hangzhou 310014, P. R. China.

Keywords: self-assembly, carbon superstructure, ultrastable charge storage, proton-coupled redox kinetics, energy storage.

Designing ingenious and stable carbon nanostructures is critical but still challenging for use in energy storage devices with superior electrochemistry kinetics, durable capacitive activity, and high rate survivability. To pursue the objective, a simple self-assembly strategy is developed to access carbon superstructures built of nanoparticle embedded plates. The carbon precursors, 2,4,6-trichloro-1,3,5-triazine and 2,6-diaminoanthraquinone can form porous organic polymer with "protic salt"-typed rigid skeleton linked by $-NH_2^+Cl^-$ "rivets", which provides the cornerstone for hydrogen-bonding-guided self-assembly of the organic backbone to superstructures by π–π plane stacking. The ameliorative charge density distribution and decreased adsorption energy in as-fabricated carbon superstructures allow the high accessibility of the build-in protophilic sites and efficient ion diffusion with a low energy barrier. Such superstructures thus deliver ultra-stable charge storage and fast proton-coupled redox kinetics at the structural−chemical defects, contributing to unprecedented lifespan (1,000,000 cycles), high-rate capability (100 A g^{-1}) for carbon-based supercapacitors, and an ultrahigh energy density (128 Wh kg^{-1}) for Zn-ion hybrid supercapacitors. The self-assembled carbon superstructures significantly improve the all-round electrochemical performances, and hold great promise for efficient energy storage.

1. Introduction

With fascinating characteristics of abundance, high electrical conductivity, environmental benignity, and stable electrochemistry, carbon-based materials have been widely used as electrodes for energy storage devices such as supercapacitors and Zn-ion hybrid capacitors.[1] Electrical energy can be stored through reversible electrosorption of charged species at the carbon–electrolyte interface, enabling fast energy harvesting/delivering in seconds and theoretical work lifespan of more than a million cycles.[2] Crafting intrinsic heterogeneous electrochemically active sites within carbon framework can contribute additional pseudocapacitance, further boosting the energy storage performance.[3] Unfortunately, this scenario is always accompanied with sluggish electrochemistry kinetics and degenerated scaffold firmness caused by heteroatomic motifs, triggering dramatic activity loss and insufficient power/cycle durability.[4] As a result, it is difficult for the fabricated devices to achieve millions of cycles in theory. In fact, the presently reported service life of carbon-based devices is rarely more than 200,000 cycles, especially at large current rates.

The surface chemistry, although crucial, affects the charge transfer dynamics and functionality redox responses of carbon electrodes in a chemistry sensitive/influenced process only if that chemistry is accessible for the electrolyte ions.[5] Three-dimensional carbon superstructures constructed from the assembly of low-dimensional segments constitute attractive prospects for energy applications.[6] This is because the superstructures inherit the desirable features of their building blocks and gain certain extra unconventional advantages, such as exceptional skeleton robustness, more exposed electroactive sites, and fast ion transfer kinetics.[7] Therefore, it is essential to fundamentally design stable carbon superstructures to allow the high availability of heteroatomic motifs and efficient ion migration with lower energy hurdles, for comprehensively improving device performances to match the expected energy storage target.

The selection of small molecules with customized chemical structure, composition and self-assembly behavior as alternative precursors to design functionalized carbons is still an interesting and ongoing work to maximize their applications in energy storage.[7a, 8] The triazine unit, a strong electroactive building block, features with highly stable C=N covalent bonds and thus provides a high density of electroactive moieties.[9] Such structure bearing good electronic carrier ability and chemical stability harnesses unique charge-storage mechanism to enable high-kinetics, reversible-capacity, rapid-cycling devices.[10] Meanwhile, given the complementary electronic attributes, the electron-withdrawing benzoquinone unit can enable two reversible one-electron transfer reactions per carbonyl center.[11] This quinone/hydroquinone transformation brings rapid electron migration in the charge/discharge process, displaying robust redox reactivity and electrochemical reversibility to boost the energy/power delivery.[12] Therefore, such complementary molecular units combine both significant electrochemical stability and multi-electron heteroatomic chemical transfer process to fulfill efficient energy storage. In addition, quinone species containing C=O groups feature high pseudocapacitance activity, but generally suffer from unsatisfied cycle stability due to their dissolution from the electrode into the electrolyte. The conversion of monomer molecules into polymers (and carbons) can inhibit the dissolution, maintain the chemical stability and improve the cycle performance.[13] The problem left behind is how to bridge the gap between the precursors with electroactive carbonyl and triazine building blocks to stable and well-designed carbon superstructures to achieve the above goal.

Herein, a self-assembly strategy is demonstrated to design well-defined laminated organic polymers or carbon superstructures with jagged edges, based on the aromatic nucleophilic substitution reaction between 2,4,6-trichloro-1,3,5-triazine (TT) and 2,6-diaminoanthraquinone (DQ) through the grafting of $-NH_2$ and $-Cl$ (**Figure 1**a, e) followed by carbonization and activation processes using sodium cyanate as the activator. A mechanism investigation unravels the key role of $-NH_2^+Cl^-$ bridges on the growth of porous polymer nanoparticles and H-

bonding self-assembly of polymeric intermediates into the superstructures. Due to high thermal stability, the organic polymer superstructures can be readily converted into hierarchical porous carbons with maintained geometry by pyrolysis/activation. The advantages of the carbon superstructures are highlighted by the comprehensive performance improvements in carbon-based supercapacitors. Besides, a constructed Zn-ion hybrid supercapacitor, involving a carbon superstructure cathode, a zinc metal anode and an aqueous $Zn(CF_3SO_3)_2$ electrolyte, also delivers remarkable energy storage performances. Systematic characterizations coupled with kinetics analysis identify the source of the exceptional charge storage as high-kinetics ion binding at the structural−chemical defects and the proton-coupled multielectron redox process of heteroatomic motifs in the ultrastable carbon superstructures.

2. Results and Discussion

2.1. Superstructure Formation Mechanism.

The synthetic route of the carbon superstructures was mainly involving three stages: i) Formation of polymer nanoparticles by aromatic nucleophilic substitution reaction of TT/DQ (**Figure 1**a, b); ii) Self-assembly of the nanoparticles into organic polymer superstructures (**Figure 1**c); iii) Pyrolysis/activation conversion to carbon superstructures (**Figure 1**d). Due to the electron-pulling effect of the halogen bonds, and the electron-pushing ability of the amine groups, TT can couple with DQ very quickly (~1 min) to yield polymer nanoparticles (~70 nm) possessing hexameric "protic salt"-like conjugated skeleton bridged by $-NH_2^+Cl^-$ groups (**Figure 1**e, Figure S1). The quaternary ammonium salt linkers serve as the "rivets" to significantly enhance the rigidity of the polymer scaffold, which is crucial for the following self-assembly process. There are hydrogen-bonding interactions among $-NH_2^+Cl^-$ linkers and carbonyl groups within the adjacent network chains in the form of N−H···O and N−H···N (**Figure 1**f, Figure S1). This interaction promotes the π−π plane stacking of the rigid conjugated building blocks, benefiting directed chain-like self-assembly to layered superstructures with

zigzag-like edges (Figure S2). X-ray powder diffraction patterns (XRD) unravel the evolution of structural regularity of self-assembled TT-DQ polymer networks (**Figure 1**g). Such a self-assembly behavior lasts about 3 h to get stable and porous superstructures with relatively concentrated pore sizes of ~3.2 nm (**Figure 1**h, i). Finally, the porous polymers can be converted into hierarchical porous carbons with inherited superstructures via common carbonization/activation, due to the high thermal stability (**Figure 1**j–n).

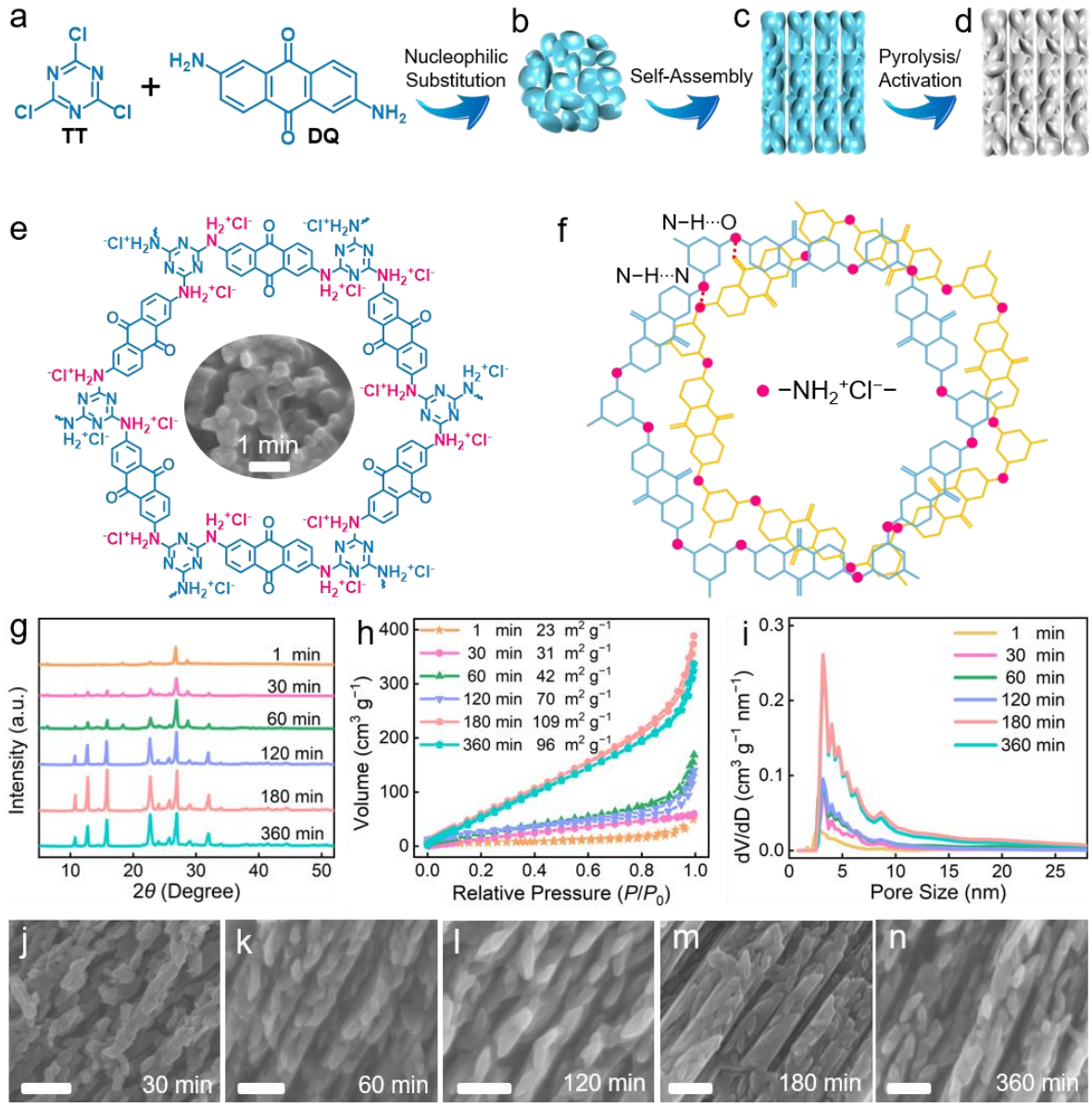

Figure 1. (a) Schematic molecular structures of TT and DQ. (b) Formation of TT-DQ polymer nanoparticles by aromatic nucleophilic substitution reaction at 1 min. (c) Self-assembly of the nanoparticles into superstructures. (d) Pyrolysis/activation conversion to carbon superstructures.

(e) TT-DQ nanoparticles (inset) with “protic salt”-like conjugated framework. (f) Schematic illustration of hydrogen-bond interaction among $-NH_2^+Cl^--$ linkers and carbonyl groups. (g) XRD patterns, (h) N_2 sorption isotherms and (i) pore size distributions of TT-DQ organic polymer superstructures obtained at different reaction times. (j−n) SEM images of carbon superstructures obtained after pyrolysis/activation. Scale bar: 200 nm.

It is inferred that rigid $-NH_2^+Cl^--$ bridges are the footstone for the self-assembly of polymeric intermediates to the superstructures. To prove this, triethylamine (TEA) was added to the reaction system to remove HCl from $-NH_2^+Cl^--$ linkers of TT-DQ (**Figure 2**a), which would result in the formation of −NH− linkers (**Figure 2**b) between TT and DQ. XPS spectra also reveals the absence of Cl element in the resultant organic polymer (**Figure 2**c). High flexible −NH− linkers cause the intertwist of the polymer chains and thus lead to the deformation of TT-DQ framework. XRD patterns (**Figure 2**d) indicate much less regular skeleton structure of TT-DQ compared with those shown in **Figure 1**f. As a result, the lack of rigid $-NH_2^+Cl^--$ linkers is unfavorable for the plane π-π stacking to get regular superstructures. The as-synthesized flexible TT-DQ polymer with −NH− linkers exhibits disordered morphologies at the polymerization times of 1 and 180 min (**Figure 2**e-f), and inferior pore structure (**Table S1**).

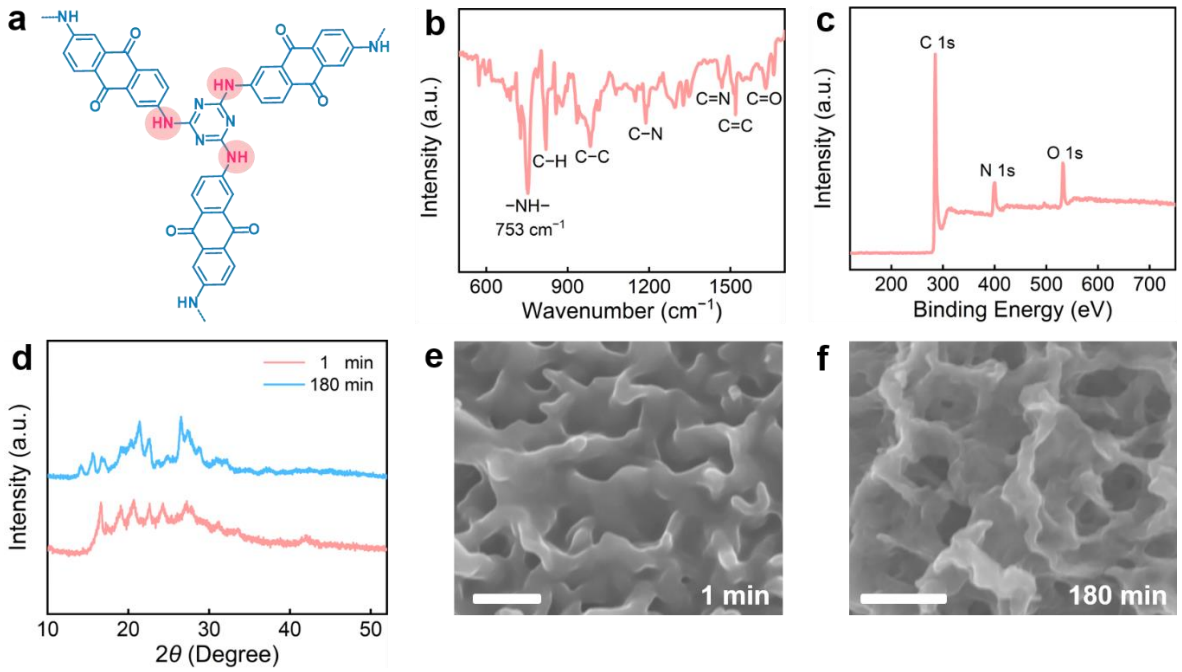

Figure 2. (a) Schematic skeleton structure, (b) FT-IR spectrum, (c) wide-scan XPS spectra, (d) XRD patterns, and (e, f) SEM images of TT-DQ polymer synthesized with the addition of TEA. Scale bar: 500 nm.

2.2. Physicochemical Characterization of Carbon Superstructures.

In addition to topology, the pore structure and surface chemistry of the carbon superstructures derived from different polymerization times were further studied. The nitrogen sorption isotherms with a rapid adsorption at low relative pressure and a hysteresis loop at middle-pressure region (**Figure 3**a) reveal the micro-, and mesoporous texture (**Figure 3**b).[14] The carbon superstructures exhibit ultrahigh surface areas (up to 1993 m^2 g^{-1}, Table S2) and hierarchical pore structure, which offer ample adsorption sites and highly open channels and thus are expected to enhance the electrolyte transport kinetics and charge storage capability.[15] In the carbon superstructures, N and O species are homogeneously distributed in the skeleton (Figure S3). X-ray photoemission spectroscopy (XPS, **Figure 3**c) identifies high contents of N (6.49−10.22 wt.%) and O (5.04−7.81 wt.%) elements (Table S2). The N 1s signal of the carbon superstructures (obtained by polymerization of 180 min follow by carbonization/activation) are fitted by three peaks (**Figure 3**d) assigned to the pyridinic nitrogen at 398.2 eV (N-6, 37.4%),

the pyrrolic nitrogen at 400.3 eV (N-5, 34.5%), and the quaternary nitrogen at 401.8 eV (N-Q, 28.1%).[16] Three typical peaks at 531.6, 531.92, and 533.64 eV are observed in O 1s spectra (**Figure 3**d), corresponding to O-1 (C=O, 69.1%) and O-2 (C-OH/C-O-C, 30.9%) groups.[17]

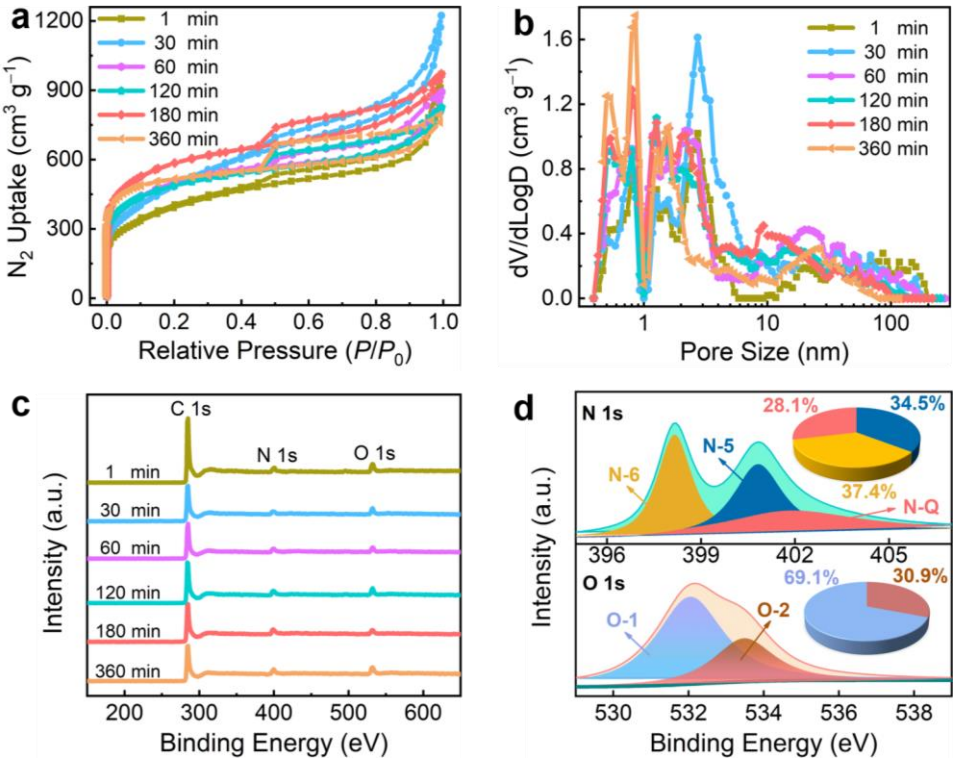

Figure 3. (a) N_2 sorption isotherms, (b) pore size distributions, and (c) XPS survey spectra of carbon superstructures derived from different polymerization times, and (d) high-resolution N 1s and O 1s XPS spectra (inset: relative content of heteroatomic species) of the carbon superstructures.

2.3. Electrochemical Energy Storage Kinetics.

The electrochemical performances of the carbon superstructures for H^+-hosting supercapacitors were investigated. Highly symmetric galvanostatic charge/discharge (GCD) profiles (**Figure 4**a, Figure S4) reveal superior electrochemical reversibility and charge storage behaviors of the carbon devices.[18] Benefiting from the well balance between geometry merit, pore structure parameters and functionality (Table S2), the optimal carbon superstructures originated from the polymerization time of 180 min delivers the highest electrode capacitance

of 468 F g^{-1} at 1 A g^{-1}. We calculated the respective capacitance contribution from electrical double layer capacitances (C_E) and pseudocapacitance (C_P).[19] From GCD data (1−100 A g^{-1}), the C_E value is 314 F g^{-1}, and the C_P contribution is 154 F g^{-1}, accounting for 32.9% of the total electrode capacitance (Figure S5a), which proves high redox activity of the retained heteroatom functionalities after carbonization. A remarkable capacitance of 269 F g^{-1} is still maintained at 100 A g^{-1}, demonstrating a superior large-current tolerance. Attracted by high capacitance and rate capability, the detailed capacitive storage behaviors of the assembled supercapacitors were studied by cyclic voltammetry (CV) curves based on the Dunn method (see Supporting Information Section S4 for details).[20] Quasi-rectangular shapes with two redox couples are observed (**Figure 4**b), which are linked to the ion-adsorption behavior and heteroatomic redox reactions of nitrogen species and carbonyl groups.[21] Two pairs of redox peaks at 0.37/0.32 and 0.49/0.44 V are attributable to the quinone/hydroquinone switching and pyridinic/pyrrolic nitrogen response.[21, 22] Upon increasing the scan rate from 10 to 500 mV s^{-1}, CV profiles remain rectangular, with only slight shifted redox peaks, substantiating the accelerated ion/electron transfer dynamics and boosted redox reaction reversibility even at large scan rates.[23] The current density (i) and the scan rate (v) of a supercapacitor follow the relationship of $i = kv^b$, where the power-law exponent of b is a vital index to estimate the charge-storage dynamics. Generally, the b value of 0.5 corresponds to sluggish reaction kinetics, while b = 1 signifies an ideal supercapacitor with ultrarapid reaction kinetics.[24] By plotting the log i against the log v, the b-values can be determined to be 0.98−0.99 for typical oxidation (O)/reduction (R) peaks in the scan-rate range of 10−500 mV s^{-1} (**Figure 4**c), corroborating the ultra-fast charge-storage kinetics of the carbon-based device. Almost 99.7% of the total stored charge is achieved by fast-kinetics process at 500 mV s^{-1} (Figure S6), which include the electric double-layer capacitance and the most surface faradic pseudocapacitance,[5c, 20a] confirming that the energy can be easily stored and delivered. The capacitive contribution from the fast-kinetics processes distinctly dominates that of the slow-kinetics processes at all scanning rates (**Figure**

4d). The slow electrode capacitance gradually decays with the increase of scan rates due to charge-transfer limited or diffusion-controlled inner Faraday reactions,[25] while rapid-capacitance remains unchanged (367 F g^{-1}).

Even at higher mass loadings (25 and 50 mg cm^{-2}), as-fabricated supercapacitors still deliver very low ion diffusion resistances of 0.20−0.23 Ω (Figure S7), small relaxation time constants of 0.47−0.83 s (**Figure 4**e), and ultrafast electrochemical capacitance storage (Figure S8 and Table S3). Moreover, the assembled supercapacitors exhibit high capacitive storage of 350−418 F g^{-1} at 1 A g^{-1}, remarkable survivability at 100 A g^{-1} (**Figure 4**f, Table S4) and cycle stability (Figure S9) even at ultrahigh active substance loadings, highlighting the ultrarapid ion/charge migration kinetics. The outstanding supercapacitive activity profit from the well-orchestrated carbon superstructures, which acts as stable interconnected conductive networks during the high-rate charge/discharge process to boost the electron conduction along the layered skeleton topography and push ion permeation inside the electroactive voids. Besides, the assembled supercapacitor with the active substance loading of 10 mg cm^{-2} displays a notable increment of initial capacitance running up to 60,000 cycles, which can be assigned to the greatly enhanced accessibility of redox-active centers by electrolyte protons. More encouragingly, the device holds 93.1% capacitance retention and a coulombic efficiency approaching to 100% when the serve term is extended to 1,000,000 cycles (**Figure 4**g). Post mortem characterizations of the carbon superstructures after cycling by SEM, EIS, and XPS spectra suggests the excellent stability of the carbon superstructures (inset of **Figure 4**g, Figure S10). To the best of our knowledge, the ultralong-term work lifespan reported here are unprecedented for carbon-based supercapacitors (Table S5). The boosted carbon/ion interface compatibility further extend the highly electroactive carbon superstructures to different types of electrolytes (Figure S11, 12) for building high energy supercapacitors (up to 113.8 Wh kg^{-1}). Notably, the overall performances of the assembled carbon-based supercapacitors substantially outclass those of

recently reported devices, not only referring to the durable capacitive activity, but also concerning the high-rate cyclability (Table S5).

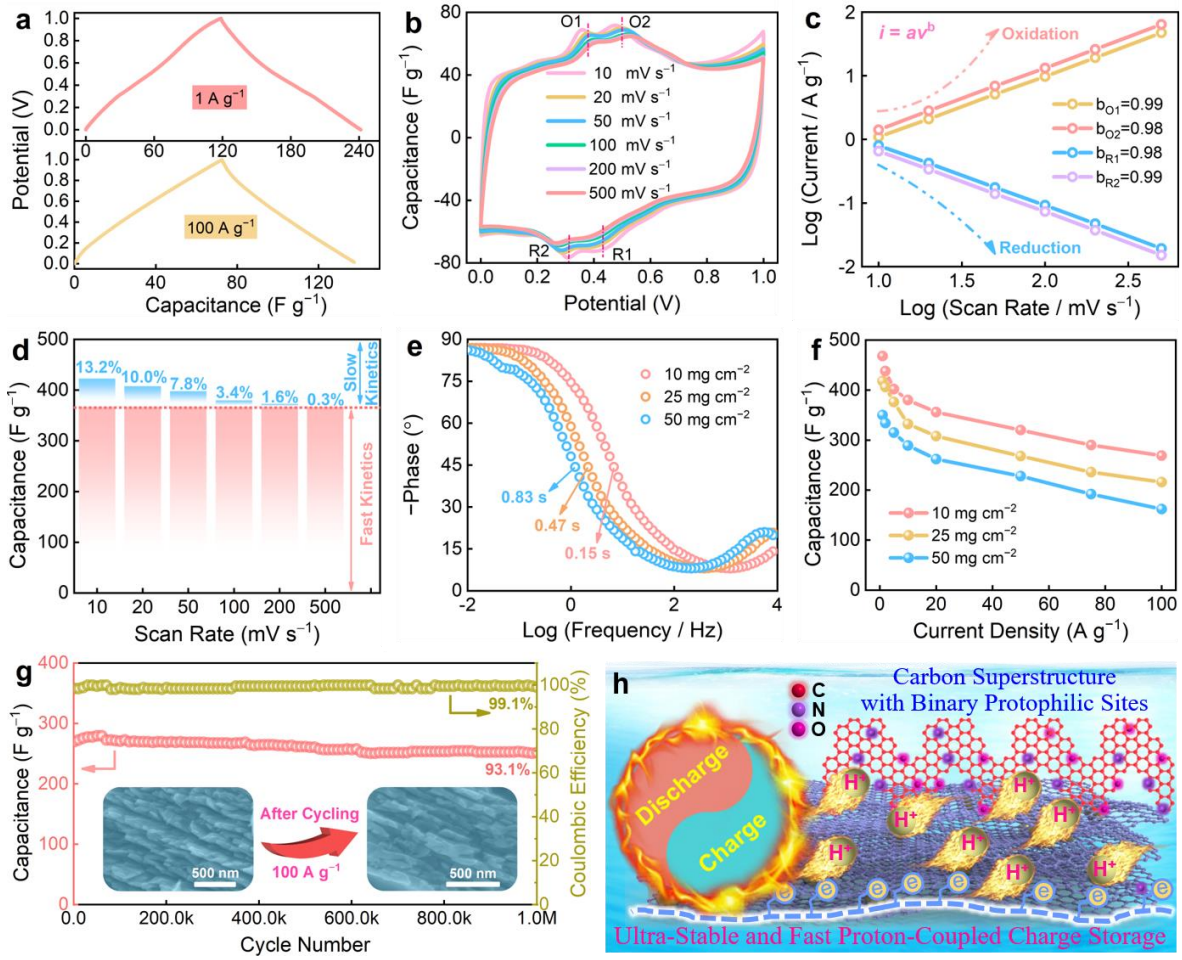

Figure 4. Electrochemistry characterizations of the assembled optimal carbon-based supercapacitors in 1 mol L^{-1} H_2SO_4 electrolyte. (a) GCD curves, (b) CV profiles, (c) the fitting plots between log*i* and log*v*, and (d) the electrode capacitance contribution from fast/slow kinetics responses at 10 mg cm^{-2}. (e) Bode plots and (f) rate capability under different mass loadings. (g) Stability over one million cycles (inset: SEM images before and after cycling). (h) A schematic illustration of proton-driven charge storage mechanism for the self-assembled carbon superstructures.

2.4. Heteroatomic Transformation Mechanism.

The fabricated carbon-based supercapacitors demonstrate excellent supercapacitive activity and durability, due to unique structural and functional design (**Figure 4**h). To better

comprehend the relationship between the electrochemical functionality and the charge storage mechanisms of carbon superstructures, we further performed ex situ XPS tests at multiple discharging/charging states based on a typical GCD curve (**Figure 5**a) to capture more chemical transformation details of heteroatomic motifs. N-6 and O-1 species gradually decrease in the process of 1−0 V discharging and nearly return back to the original value during 0−1 V charging, while N-5 resonance peak undergoes a reverse variation trend (**Figure 5**b, c). In contrast, N-Q without electrochemical activity is basically unchanged. These results verify that reversible switching reactions of N-6, N-5 and O-1 take place via the chemical interactions with H^+ during the full discharging/charging processes. Ex situ potential-dependent EIS of the carbon-based supercapacitors was also monitored to analyze ion diffusion resistivity and electron transport dynamics during the heteroatomic chemical transformation process, as shown in **Figure 5**d, e. Very low ion transport resistances (R_s=0.18−0.31 Ω, Table S6) during the cycling confirm the fast charge-transfer kinetics. During discharging, R_s and R_{ct} are on a voltage-driven downward trend. H^+ diffusion resistivity (σ) and transmission coefficient (D_{H^+}) can be calculated based on the equations given in Supporting Information Section S5. There is a lessening trend in σ from 0.96 to 0.64 Ω $s^{-0.5}$, accompanying with the enlargement of D_{H^+} from 1.23×10^{-8} to 2.77×10^{-8} cm^2 s^{-1} (**Figure 5**f, Table S6). The values of R_s/R_{ct} and σ/D_{H^+} get back during the charging process (**Figure 5**e, g). This result demonstrates reversible ion-kinetics transformation behaviors within the functionalized superstructure host, and low operation potentials promote H^+ diffusion to the electrode/electrolyte interface for the transformation of electroactive N/O species.

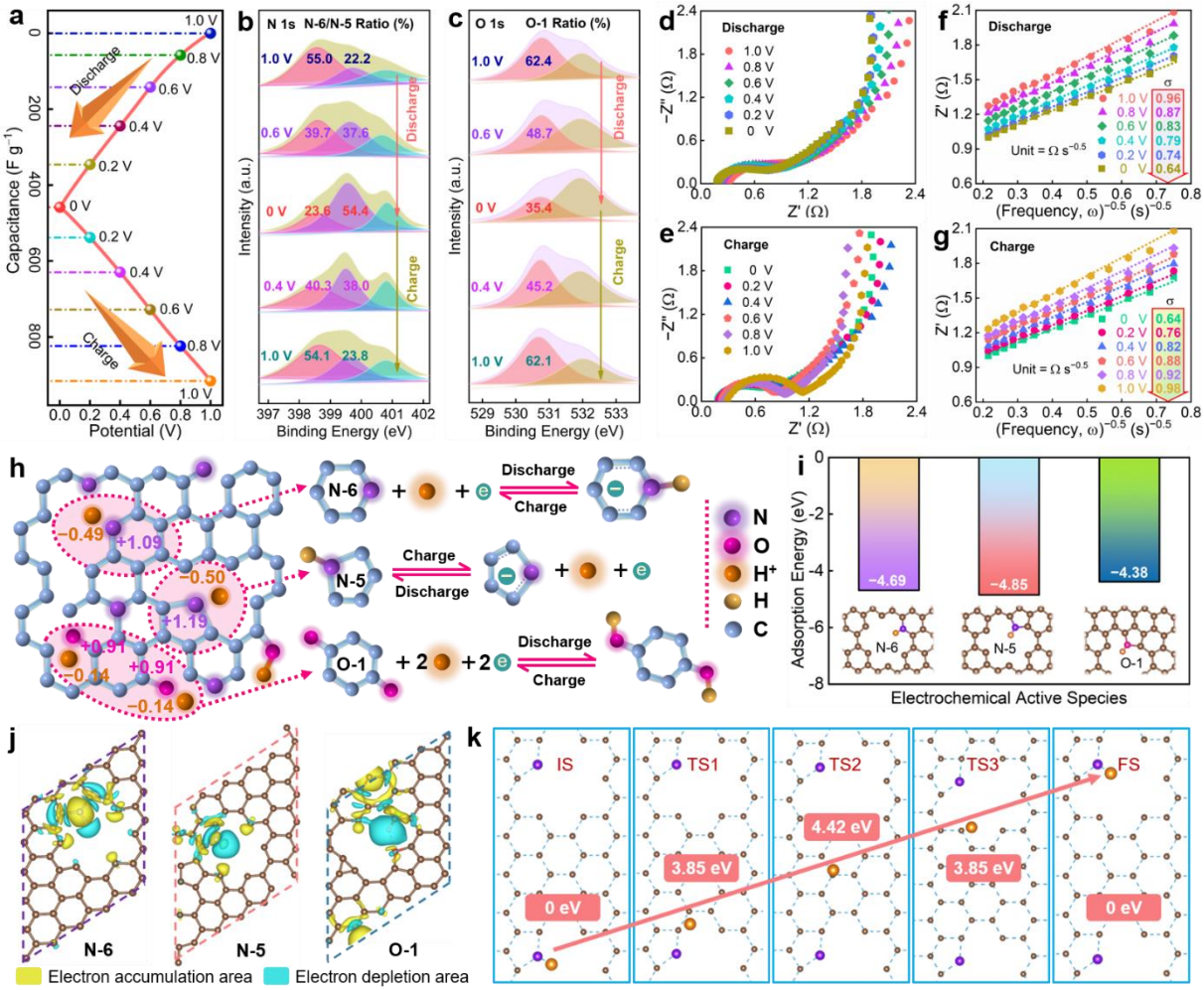

Figure 5. Heteroatomic chemical transition in the proton storage process. (a) A GCD profile. Ex situ (b) N 1s and (c) O 1s XPS spectra, and (d, e) Nyquist plots and (f, g) the corresponding relationship between Z' and $\omega^{-0.5}$ in intermediate frequency region at various discharging/charging states. (h) Bader charge analysis for electroactive surface defects and the redox reactions of heteroatomic species. (i) The calculated relative adsorption energy and (j) the electron density differences of H adsorbed on the optimized N-6, N-5, O-1 active sites. The increased electron density and decreased electron density are represented by the yellow and green regions, respectively. (k) Top view of H ion diffusion in N-5 doping structure (path 2) and the corresponding diffusion barrier energies at various states of initial state (IS), transition state (TS1, TS2, TS3) and final state (FS).

Besides, Bader charge analysis was performed to unravel the chemical interaction between electrolyte ion and introduced active sites within the carbon matrix. Negative net charges of H (−0.49 eV corresponding to N-6 and −0.50 eV to N-5) indicate that the electron of H tends to be delocalized (lost). They thus tend to flow toward N-6/N-5 (+1.19 and +1.09 eV) to form stable configurations, embodying the strong chemical interaction between electroactive nitrogen sites and H^+ ions (**Figure 5**h).[26] Particularly, N-6/N-5 species bearing a lone electron pair for conjugation with the π-conjugated rings drive the interconversion between =N− and −NH− during the charge/discharge process.[27] There are also significant charge shifts from H (−0.14 eV) to electron-withdrawing quinone-type O-1 (+0.91 eV), being beneficial to yield surface adsorption-induced pseudocapacitive response. This process triggers the availability of more H^+ around N-6, N-5 and O-1 active centers and drives the proton-coupled reversible redox switch, bringing enhanced electrochemical energy storage.[28]

The first-principles simulation based on the density functional theory (DFT) method was performed to further elucidate the above experimental results. The adsorption ability of H ion is remarkably strengthened to achieve a relative adsorption energy (ΔE_a) of −4.69 and −4.85 eV for N-6 and N-5 sites (**Figure 5**i). This result infers that both active species are more energy-favorable for H^+ chemisorption to trigger pseudocapacitive reactions and modulate the electronic structure for facilitating the electron transfer within the carbon matrix.[29] The capture ability of O-1 to H atoms is boosted to deliver a binding energy of −4.38 eV (**Figure 5**i), indicating the robust electrochemically reactivity of carbonyl group.[30] In addition, top (**Figure 5**j) and side (Figure S13) views of the electron density difference were demonstrated by subtracting the charge densities of H and C atoms from N-6, N-5 and O-1 to understand the bonding nature of the adsorbed H atoms in depth. The charge depletion of H and much charge accumulation around N/O active regions are explicitly observed. A net gain of charge in these heteroatom species suggests the charge transfer tendency from the adsorbed H to the nearest C atoms, which signifies that N/O significantly boost the affinity between electrolyte ions and

heteroatom-substituted carbons.[31] This finding illuminates that heteroatomic motifs throughout the carbon superstructures can effectively lower the energy barrier of chemical interactions between electroactive sites and protons, boosting the proton-driven charge storage process. Besides, the minimum diffusion energy paths of H ions in different models are displayed in Figure S14. The diffusion barriers at different transition states in-between the carbon layers are presented in **Figure 5**k. It should be noted that H atoms delivers a lower diffusion energy barrier of 4.42 eV for path 2 model compared with path 1 model (6.11 eV, Figure S15), expediting the migration of electrolyte ions on electrochemically active sites. Therefore, decreased ion-binding energy barrier and enhanced electronegativity of the carbon superstructures benefit the formation/fracture of C−N−H and C−O−H configurations, highlighting more possibilities to yield high-kinetics proton-storage capability and exceptional cyclability.

2.5. Proton-Assisted Zn-Ion Storage in Carbon Superstructures.

We further constructed a Zn-ion hybrid supercapacitor by employing zinc metal as the anode and carbon superstructures as the cathode in aqueous $Zn(CF_3SO_3)_2$ electrolyte. The Zn-ion device synergizes the energy storage mechanisms of supercapacitors with rapid ion adsorption/desorption processes and batteries with faradaic reversible reactions,[32] which are expected to achieving high energy-power delivery and long-life performance. Three identical assembled Zn-ion devices exhibit the same GCD charge/discharge behavior (Figure S16 and **Figure 17**). The fabricated device exhibits a high capacity of 198 mA h g^{-1} at 0.5 A g^{-1}, together with a reversible capacity of 120 mA h g^{-1} at 50 A g^{-1}. Besides, the voltage drop reflected by GCD curves is only 0.09 V at a high current density level of 50 A g^{-1}, evidencing that the introduction of heteroaromatic species is capable of significantly enhancing electrical conductivity and promoting ion/electron transport dynamics.[33] Moreover, the device capacity is switched back to 196 mA h g^{-1} after 70 successive cycles at various current rates (Figure

S17). To describe the degree of capacitive effect of the device, the surface-driven capacitive and diffusion-controlled energy storage processes were investigated (Figure S18), which suggest the rapid-capacitive dominated charge storage with a certain degree of diffusion-controlled redox reactions.[34] More encouragingly, the aqueous Zn//carbon device achieves an ultrahigh energy density of 128 Wh kg^{-1} at 327 W kg^{-1} (based on the mass of carbon cathode), outperforming most previously reported Zn-based hybrid devices (**Figure 6**a).[1f, 2a, 4a, 32, 35] A high power density of 29.7 kW kg^{-1} with a corresponding energy density of 70.6 Wh kg^{-1} can be obtained at 50 A g^{-1}, showing high energy/power delivery. Presently, many reported Zn-ion devices with high energy densities are generally estimated without considering the mass of Zn-anode. Based on the total weight of zinc anode and carbon cathode, the fabricated Zn-ion device shows an energy density of 20.9 Wh kg^{-1}, 1.3 times of most recently reported value (16.2 Wh kg^{-1}).[35d] Besides, the device shows a prolonged cycling performance with 91.8% capacity retention and 99.6% coulombic efficiency over 200,000 cycles at 40 A g^{-1} (**Figure 6**b). SEM images of the carbon cathode after cycling (Figure S19) indicate the superb strutural stability of the carbon superstructures in the hybrid supercapacitor.

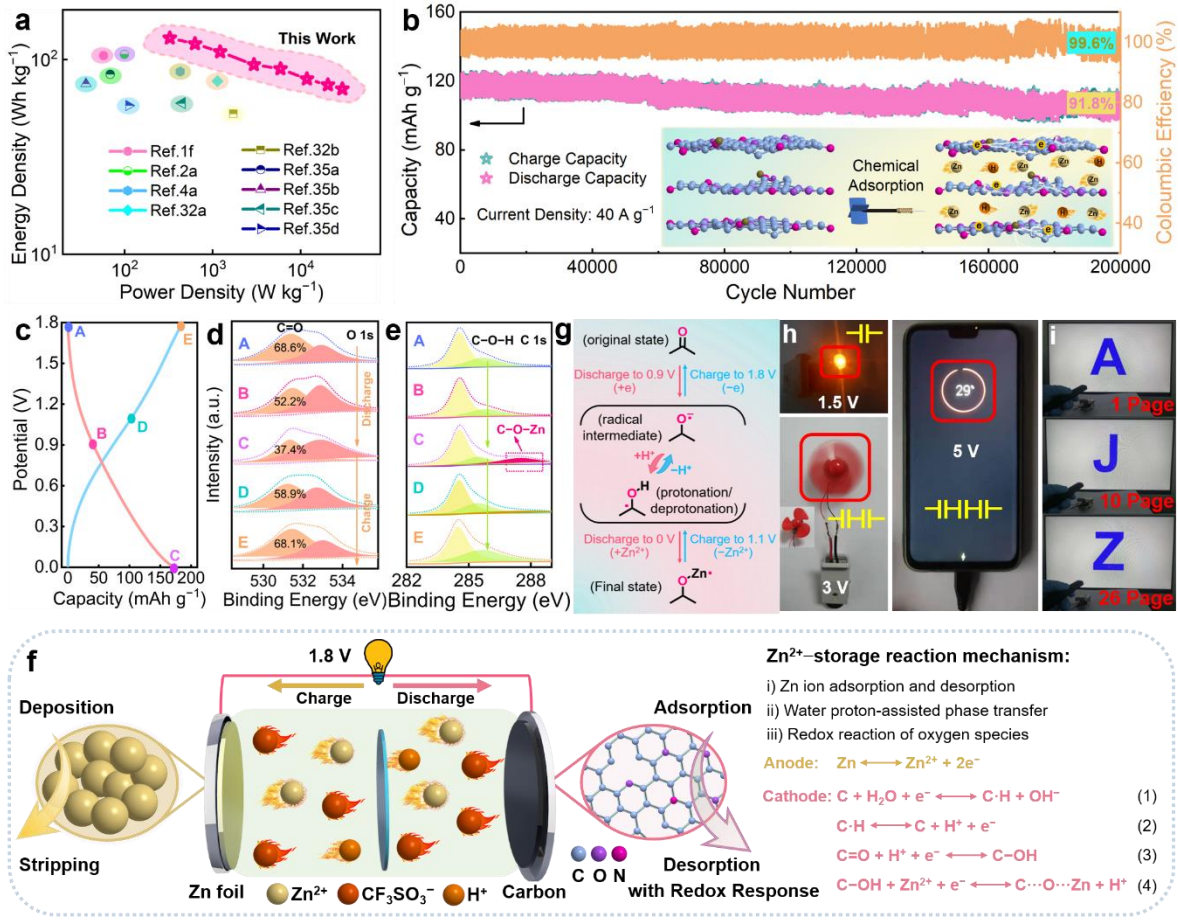

Figure 6. Electrochemical performances of the assembled Zn-ion device. (a) Ragone plots. (b) Stability after 200,000 cycles. (c) A typical GCD curve at 2 A g^{-1} and corresponding ex situ (d) O 1s and (e) C 1s XPS spectra of the carbon cathode at various charge/discharge states. (f) Schematic illustration of device configuration and charge-storage mechanism. (g) The redox reaction mechanism. (h) Photographs presenting successful operation of three different electronic devices: LED lamp (1.5 V), miniature fan (3 V) and mobile phone (5 V) by connecting 1−3 devices in series. (i) A laser pointer (3 V) powered by two Zn-ion devices continuously presenting 26-page slides for more than 60 minutes.

Zn^{2+} cations are widely recognized as efficient active ions stored in carbon cathode,[2a, 36] but it is still unknown whether protons are active during Zn-ion storage. In view of the mildly acidic environment of $Zn(CF_3SO_3)_2$ electrolyte (pH=4.12) and the smaller size of hydrated protons,[3a] investigation of the role of H^+ is essential to better understand the Zn-ion storage mechanism. Therefore, we performed comparative electrochemical experiments and a series of ex-situ

characterizations. An aqueous HCF_3SO_3 solution with the same pH of $Zn(CF_3SO_3)_2$ was employed as the electrolyte to explore the possible participation of H^+ during Zn^{2+} storage (Figure S20a). HCF_3SO_3-based device presents a capacity of 40 mAh g^{-1}, which suggest that hydrogen ions take part in the cathodic electrochemical reaction of the device. With the increase of the concentration of H^+ (pH value from 6.32 to 1.02), the device capacities significantly boost from 6 to 94 mAh g^{-1} (Figure S20b, c). This result further indicates that protons take part in the electrochemical reaction of the carbon cathode. Besides, ex-situ high-resolution O 1s XPS spectra was performed to track the surface variations of the carbon cathode at the discharging state of 0 V in hybrid Zn-ion device using HCF_3SO_3 electrolytes with different pH values (1.02−6.32). The contents of carbonyl groups reduce gradually with the decrease of pH values (Figure S20d), which indicates that more carbonyl functional groups are chemically consumed by more H^+, supporting the redox process between C=O and H^+ in Equation (3) of **Figure 6**f.

Ex situ XPS measurement at different voltages (**Figure 6**c) was performed to track the surface variations of the carbon cathode. Electrochemical hydrogen adsorption/desorption leads to a dynamic local alkaline environment (**Figure 6**f, Equation (1)),[1f] in which OH^- anions strongly coordinate with Zn^{2+} to form $Zn(CF_3SO_3)_2[Zn(OH)_2]_3{\cdot}xH_2O$ product (confirmed by XRD analysis, Figure S21).[2c] While the generated H^+ cations (**Figure 6**f, Equation (2)) diffuse into carbon cathode to account for the reversible redox reactions of oxygen species.[37] During the discharging from 1.8 to 0.9 V, C=O groups in carbon cathode is continuously reduced to C−OH (**Figure 6**d) by gaining protons and electrons (Equation (3)). Meanwhile, H^+ and Zn^{2+} ions are transferred to carbon cathode at the solid−liquid interface, named as C−Zn(H). With the proceeding of the discharging to 0 V, the C−Zn(H) further undergoes a metathesis of Zn^{2+} and H^+ with more activated C=O groups, where the protons transferred from water are released back into the electrolyte, finally yielding C−O−Zn configuration[38] (**Figure 6**e, f, Equation (4), Fig. S22). During the charging, the reversibility of this process is followed. The chemical variations of O species could be a positive proof of the co-uptake of H^+ and Zn^{2+}. The overall

proton-assisted Zn-ion charge-storage mechanism within ultrahigh-rate superstructure host is depicted in **Figure 6**g, involving reversible electrochemical hydrogen adsorption/desorption and conversion in oxidation states of oxygen species during each round-trip charge−discharge cycle. Element mapping images (Figure S23) also reveal the highly reversible formation/dissolution transition of $Zn(CF_3SO_3)_2[Zn(OH)_2]_3{\cdot}xH_2O$, supporting the adsorption/release behaviors of protons at the discharge/charge process (Table S7). The Zn-ion hybrid device configuration and overall reaction mechanism are depicted in **Figure 6**f. Three different electronic devices, 1.5 V light-emitting-diode (LED) lamp, 3 V miniature fan and 5 V mobile phone, were successfully powered by connecting the constructed Zn-ion hybrid supercapacitors in series (**Figure 6**h). Besides, two Zn-ion devices in series can successfully drive an electronic laser presenter (3 V working voltage) to present 26-page slides constantly for more than 60 min (**Figure 6**i), due to the good energy storage capability of the device.

For both the supercapacitor and Zn-ion hybrid device applications, the structural and functional design of carbon superstructures contribute to the all-round performance improvements in terms of supercapacitive activity and durability. Firstly, robust carbon superstructures with excellent mechanical strength can prevent skeleton deformation under large-current cycling rates and minimize the ion/electron transport obstruction within the whole carbon scaffold, forcing the achievement of ultrarapid reaction kinetics and ultrastable longevity. Secondly, large surface area and multi-scale porosity of carbon scaffold afford ample ion-interaction platforms for promoting chemical adsorption process, and allow the high accessibility of the build-in protophilic sites and efficient ion transport with low energy barriers. Thirdly, rich heteroatomic motifs dispersed throughout the carbon superstructures afford dense redox-active sites bonded to electrolyte cations, which trigger proton-driven high-rate redox kinetics to supplement remarkable pseudocapacitance storage/delivery. Their synergism optimizes the supercapacitive performances and further elevating the energy/power supplies of carbon superstructures to superior levels.

3. Conclusion

In conclusion, a self-assembly strategy is demonstrated to design carbon superstructures derived from TT-DQ. Structural evolution investigation untangles the key roles of $-NH_2^+Cl^--$ bridges and hydrogen-bonding interaction on the self-assembly process of polymeric intermediates into rigid polymer superstructures and carbon derivatives. With prominent merits in superstructures, the fabricated carbon-based supercapacitor features excellent electrochemical performance in terms of ultrahigh rate performance (269 F g^{-1} at 100 A g^{-1}) and long-life cyclability (93.1% capacitive activity after 1,000,000 cycles at 100 A g^{-1}). Significantly, an aqueous Zn-ion hydrid supercapcitor delivers an ultrahigh energy density of 128 Wh kg^{-1} and an ultralong duration of 91.8% retention over 200,000 cycles at 40 A g^{-1}. Marriage of comprehensive characterizations and dynamic analysis illustrate that functionalized carbon superstructures can effectively lower the ion-binding energy barriers at the structural−chemical defects, promoting proton-coupled charge storage on the electrode surface. This work offers a new insight in the improvement of charge storage performance through design of structure engineering and surface chemistry.

Supporting Information
Supporting Information is available from the Wiley Online Library or from the author.

Acknowledgements
This work is financially supported by the National Natural Science Foundation of China (Nos. 21875165, 51772216, and 21905207), the Science and Technology Commission of Shanghai Municipality, China (20ZR1460300, 14DZ2261100), Zhejiang Provincial Natural Science Foundation of China (No. LY19B010003), and the Fundamental Research Funds for the Central Universities. The authors are grateful to the University of Strasbourg and the CNRS.

Received: ((will be filled in by the editorial staff))
Revised: ((will be filled in by the editorial staff))
Published online: ((will be filled in by the editorial staff))

Conflict of Interest
The authors declare no conflict of interest.

References

[1] a) M. Yu, N. Chandrasekhar, R. K. M. Raghupathy, K. H. Ly, H. Zhang, E. Dmitrieva, C. Liang, X. Lu, T. D. Kuhne, H. Mirhosseini, I. M. Weidinger, X. Feng, *J. Am. Chem. Soc.* **2020**, *142*, 19570; b) H. Zhang, Q. Liu, Y. Fang, C. Teng, X. Liu, P. Fang, Y. Tong, X. Lu, *Adv. Mater.* **2019**, *31*, 1904948; c) C. Cui, Y. Gao, J. Li, C. Yang, M. Liu, H. Jin, Z. Xia, L. Dai, Y. Lei, J. Wang, S. Wang, *Angew. Chem. Int. Ed.* **2020**, *59*, 7928; d) K. Nomura, H. Nishihara, N. Kobayashi, T. Asada, T. Kyotani, *Energy Environ. Sci.* **2019**, *12*, 1542; e) K. Tian, J. Wang, L. Cao, W. Yang, W. Guo, S. Liu, W. Li, F. Wang, X. Li, Z. Xu, Z. Wang, H. Wang, Y. Hou, *Nat. Commun.* **2020**, *11*; f) J. Yin, W. Zhang, W. Wang, N. A. Alhebshi, N. Salah, H. N. Alshareef, *Adv. Energy Mater.* **2020**, *32*, 2001705.

[2] a) S. Wu, Y. Chen, T. Jiao, J. Zhou, J. Cheng, B. Liu, S. Yang, K. Zhang, W. Zhang, *Adv. Energy Mater.* **2019**, *9*, 1902915; b) H. Song, J. Su, C. Wang, *Adv. Energy Mater.* **2021**, *11*, 2003685; c) Z. Li, D. Chen, Y. An, C. Chen, L. Wu, Z. Chen, Y. Sun, X. Zhang, *Energy Storage Mater.* **2020**, *28*, 307; d) T. Wang, Y. Sun, L. Zhang, K. Li, Y. Yi, S. Song, M. Li, Z. A. Qiao, S. Dai, *Adv. Mater.* **2019**, *31*, 1807876; e) J. Cui, J. Yin, J. Meng, Y. Liu, M. Liao, T. Wu, M. Dresselhaus, Y. Xie, J. Wu, C. Lu, X. Zhang, *Nano Lett.* **2021**, *21*, 2156.

[3] a) Y. Wang, C. Wang, Z. Ni, Y. Gu, B. Wang, Z. Guo, Z. Wang, D. Bin, J. Ma, Y. Wang, *Adv. Mater.* **2020**, *32*, 2000338; b) Y. Zhang, S. Yang, S. Wang, X. Liu, L. Li, *Energy Storage Mater.* **2019**, *18*, 447; c) W. Fan, J. Ding, J. Ding, Y. Zheng, W. Song, J. Lin, C. Xiao, C. Zhong, H. Wang, W. Hu, *Nano-Micro Lett.* **2021**, *13*, 59; d) T. Lv, M. Liu, D. Zhu, L. Gan, T. Chen, *Adv. Mater.* **2018**, *30*, 1705489; e) C. Liu, X. Huang, J. Wang, H. Song, Y. Yang, Y. Liu, J. Li, L. Wang, C. Yu, *Adv. Funct. Mater.* **2018**, *28*, 1705253.

[4] a) Y. Lu, Z. Li, Z. Bai, H. Mi, C. Ji, H. Pang, C. Yu, J. Qiu, *Nano Energy* **2019**, *66*, 104132; b) H. Jin, X. Feng, J. Li, M. Li, Y. Xia, Y. Yuan, C. Yang, B. Dai, Z. Lin, J. Wang, J. Lu, S. Wang, *Angew. Chem. Int. Ed.* **2019**, *58*, 2397.

[5] a) F. Hu, T. Zhang, J. Wang, S. Li, C. Liu, C. Song, W. Shao, S. Liu, X. Jian, *Nano Energy* **2020**, *74*, 104789; b) Y.-Y. Liu, X.-C. Li, S. Wang, T. Cheng, H. Yang, C. Liu, Y. Gong, W.-Y. Lai, W. Huang, *Nat. Commun.* **2020**, *11*, 5561; c) Y. Lu, J. Liang, S. Deng, Q. He, S. Deng, Y. Hu, D. Wang, *Nano Energy* **2019**, *65*, 103993; d) H. Tang, J. Yao, Y. Zhu, *Adv. Energy Mater.* **2021**, *11*, 2003994.

[6] a) Y. Zhu, L. Li, C. Zhang, G. Casillas, Z. Sun, Z. Yan, G. Ruan, Z. Peng, A. R. Raji, C. Kittrell, R. H. Hauge, J. M. Tour, *Nat. Commun.* **2012**, *3*, 1225; b) S. Nardecchia, D. Carriazo, M. L. Ferrer, M. C. Gutierrez, F. del Monte, *Chem. Soc. Rev.* **2013**, *42*, 794.

[7] a) Z. Xu, X. Zhuang, C. Yang, J. Cao, Z. Yao, Y. Tang, J. Jiang, D. Wu, X. Feng, *Adv. Mater.* **2016**, *28*, 1981; b) S. Chen, D. M. Koshy, Y. Tsao, R. Pfattner, X. Yan, D. Feng, Z. Bao, *J. Am. Chem. Soc.* **2018**, *140*, 10297.

[8] a) J. Xu, J. Zhu, X. Yang, S. Cao, J. Yu, M. Shalom, M. Antonietti, *Adv. Mater.* **2016**, *28*, 6727; b) Y. Li, S. Zheng, X. Liu, P. Li, L. Sun, R. Yang, S. Wang, Z. S. Wu, X. Bao, W. Q. Deng, *Angew. Chem. Int. Ed.* **2018**, *57*, 7992.

[9] a) L. Li, F. Lu, R. Xue, B. Ma, Q. Li, N. Wu, H. Liu, W. Yao, H. Guo, W. Yang, *ACS Appl. Mater. Interfaces* **2019**, *11*, 26355; b) S. Zhang, S. Long, H. Li, Q. Xu, *Chem. Eng. J.* **2020**, *400*, 125898; c) C. Lu, J. Yang, S. Wei, S. Bi, Y. Xia, M. Chen, Y. Hou, M. Qiu, C. Yuan, Y. Su, F. Zhang, H. Liang, X. Zhuang, *Adv. Funct. Mater.* **2019**, *29*, 1806884.

[10] a) Y. Yuan, F. Sun, F. Zhang, H. Ren, M. Guo, K. Cai, X. Jing, X. Gao, G. Zhu, *Adv. Mater.* **2013**, *25*, 6619; b) Z. Cheng, H. Pan, H. Zhong, Z. Xiao, X. Li, R. Wang, *Adv. Funct. Mater.* **2018**, *28*, 1707597.

[11] a) R. Shi, L. Liu, Y. Lu, C. Wang, Y. Li, L. Li, Z. Yan, J. Chen, *Nat. Commun.* **2020**, *11*, 117; b) L. Wang, H. Zhang, Y. Wang, C. Qian, Q. Dong, C. Deng, D. Jiang, M. Shu, S. Pan, S. Zhang, *J. Mater. Chem. A* **2020**, *8*, 15002.

[12] a) Z. Ouyang, D. Tranca, Y. Zhao, Z. Chen, X. Fu, J. Zhu, G. Zhai, C. Ke, E. Kymakis, X. Zhuang, *ACS Appl. Mater. Interfaces* **2021**, *13*, 9064; b) H. Zhang, Y. Fang, F. Yang, X. Liu, X. Lu, *Energy Environ Sci.* **2020**, *13*, 2515.

[13] a) Z. Luo, L. Liu, J. Ning, K. Lei, Y. Lu, F. Li, J. Chen, *Angew. Chem. Int. Ed.* **2018**, *57*, 9443; b) G. Wang, N. Chandrasekhar, B. P. Biswal, D. Becker, S. Paasch, E. Brunner, M. Addicoat, M. Yu, R. Berger, X. Feng, *Adv. Mater.* **2019**, *31*, 1901478.

[14] M. Dvoyashkin, D. Leistenschneider, J. D. Evans, M. Sander, L. Borchardt, *Adv. Energy Mater.* **2021**, *33*, 2100700; b) R. Zhao, Z. Liang, S. Gao, C. Yang, B. Zhu, J. Zhao, C. Qu, R. Zou, Q. Xu, *Angew. Chem. Int. Ed.* **2019**, *58*, 1975.

[15] a) N. W. Xuan Qiu, Zhuo Wang, Fei Wang, and Yonggang Wang, *Angew.Chem. Int. Ed.* **2021**, *60*, 9610; b) L.-F. Chen, Y. Lu, L. Yu, X. W. Lou, *Energy Environ. Sci.* **2017**, *10*, 1777.

[16] W. Zhang, J. Yin, M. Sun, W. Wang, C. Chen, M. Altunkaya, A. H. Emwas, Y. Han, U. Schwingenschlögl, H. N. Alshareef, *Adv. Mater.* **2020**, *32*, 2000732.

[17] J. Yu, C. Yu, W. Guo, Z. Wang, S. Li, J. Chang, X. Tan, Y. Ding, M. Zhang, L. Yang, Y. Xie, R. Fu, J. Qiu, *Nano Energy* **2019**, *64*, 103921.

[18] a) W. Ma, W. Li, M. Li, Q. Mao, Z. Pan, J. Hu, X. Li, M. Zhu, Y. Zhang, *Adv. Funct. Mater.* **2021**, *31*, 2100195; b) Z. Song, L. Miao, L. Li, D. Zhu, L. Gan, M. Liu, *Carbon* **2021**, *180*, 135.

[19] T. Lin, I.-W. C. F. Liu, C. Yang, H. Bi, F. Xu, F. Huang, *Science* **2015**, *350*, 1508.

[20] a) T. Liu, Z. Zhou, Y. Guo, D. Guo, G. Liu, *Nat. Commun.* **2019**, *10*, 675; b) L. Miao, H. Duan, D. Zhu, Y. Lv, L. Gan, L. Li, M. Liu, *J. Mater. Chem. A* **2021**, *9*, 2714.

[21] M. Li, J. Liu, Y. Li, G. Xing, X. Yu, C. Peng, L. Chen, *CCS Chem.* 2020, *2*, 696.

[22] W. Wang, W. Zhao, T. Chen, Y. Bai, H. Xu, M. Jiang, S. Liu, W. Huang, Q. Zhao, *Adv. Funct. Mater.* **2021**, *31*, 2010306.

[23] Q. Li, Z. Dai, J. Wu, W. Liu, T. Di, R. Jiang, X. Zheng, W. Wang, X. Ji, P. Li, Z. Xu, X. Qu, Z. Xu, J. Zhou, *Adv. Energy Mater.* **2020**, *32*, 1903750.

[24] J. L. Xia, D. Yan, L. P. Guo, X. L. Dong, W. C. Li, A. H. Lu, *Adv. Mater.* **2020**, 32, 2000447.

[25] a) X. Yang, Q. Wang, K. Zhu, K. Ye, G. Wang, D. Cao, J. Yan, *Adv. Funct. Mater.* **2021**, *31*, 2101087; b) J. Yan, H. Li, K. Wang, Q. Jin, C. Lai, R. Wang, S. Cao, J. Han, Z. Zhang, J. Su, K. Jiang, *Adv. Energy Mater.* **2021**, *11*, 2003911; c) C. Costentin, J.-M. Savéant, *ACS Appl. Energy Mater.* **2019**, *2*, 4981.

[26] C. Li, Z. Sun, T. Yang, L. Yu, N. Wei, Z. Tian, J. Cai, J. Lv, Y. Shao, M. H. Rummeli, J. Sun, Z. Liu, *Adv. Mater.* **2020**, *32*, 2003425.

[27] a) D. Hulicova-Jurcakova, M. Seredych, G. Q. Lu, T. J. Bandosz, *Adv. Funct. Mater.* **2009**, *19*, 438; b) N. Wang, R. Zhou, H. Li, Z. Zheng, W. Song, T. Xin, M. Hu, J. Liu, *ACS Energy Letters* **2021**, *6*, 1141.

[28] Y. Liao, H. Wang, M. Zhu, A. Thomas, *Adv. Mater.* **2018**, *30*, 1705710.

[29] a) X. Hu, G. Zhong, J. Li, Y. Liu, J. Yuan, J. Chen, H. Zhan, Z. Wen, *Energy Environ. Sci.* **2020**, *13*, 2431; b) W. Yang, J. Zhou, S. Wang, Z. Wang, F. Lv, W. Zhang, W. Zhang, Q. Sun, S. Guo, *ACS Energy Lett.* **2020**, *5*, 1653.

[30] G. Son, V. Ri, C. Noh, H. Yoon, S. Ko, J. Moon, Y. Jung, C. B. Park, C. Kim, *ACS Energy Letters* **2021**, *6*, 1659.

[31] G. Zhao, Y. Zhang, Z. Gao, H. Li, S. Liu, S. Cai, X. Yang, H. Guo, X. Sun, *ACS Energy Lett.* **2020**, *5*, 1022.

[32] a) Z. Zhou, X. Zhou, M. Zhang, S. Mu, Q. Liu, Y. Tang, *Small* **2020**, *16*, 2003174; b) H. Wang, M. Wang, Y. Tang, *Energy Storage Mater.* **2018**, *13*, 1.

[33] a) F. Xie, H. Li, X. Wang, X. Zhi, D. Chao, K. Davey, S. Z. Qiao, *Adv. Energy Mater.* **2021**, *11*, 2003419; b) J. Huang, L. Wang, Z. Peng, M. Peng, L. Li, X. Tang, Y. Xu, L. Tan, K. Yuan, Y. Chen, *J. Mater. Chem. A* **2021**, *9*, 8435.

[34] Y. Zheng, W. Zhao, D. Jia, Y. Liu, L. Cui, D. Wei, R. Zheng, J. Liu, *Chem. Eng. J.* **2020**, *387*, 124161.

[35] a) L. Dong, X. Ma, Y. Li, L. Zhao, W. Liu, J. Cheng, C. Xu, B. Li, Q.-H. Yang, F. Kang, *Energy Storage Mater.* **2018**, *13*, 96; b) Y. Zhang, Z. Wang, D. Li, Q. Sun, K. Lai, K. Li, Q. Yuan, X. Liu, L. Ci, *J. Mater. Chem. A* **2020**, *8*, 22874; c) S. Chen, L. Ma, K. Zhang, M. Kamruzzaman, C. Zhi, J. A. Zapien, *J. Mater. Chem. A* **2019**, *7*, 7784; d) X. Qiu, N. Wang, Z. Wang, F. Wang, Y. Wang, *Angew. Chem. Int. Ed.* **2021**, *60*, 9610.

[36] P. Liu, Y. Gao, Y. Tan, W. Liu, Y. Huang, J. Yan, K. Liu, *Nano Res.* **2019**, *12*, 2835.

[37] N. Liu, X. Wu, Y. Zhang, Y. Yin, C. Sun, Y. Mao, L. Fan, N. Zhang, *Adv. Sci.* **2020**, *7*, 2000146.

[38] C. C. Hou, Y. Wang, L. Zou, M. Wang, H. Liu, Z. Liu, H. F. Wang, C. Li, Q. Xu, *Adv. Mater.* **2021**, *33*, 2101698.

Keywords: self-assembly, carbon superstructure, ultrastable charge storage, proton-coupled redox kinetics, energy storage.

Ziyang Song, Ling Miao, Laurent Ruhlmann, Yaokang Lv, Dazhang Zhu, Liangchun Li, Lihua Gan, and Mingxian Liu*

Self-Assembled Carbon Superstructures Achieving Ultra-Stable and Fast Proton-Coupled Charge Storage Kinetics

The table of contents entry

Complementary acceptor-donor molecules of 2,4,6-trichloro-1,3,5-triazine and 2,6-diaminoanthraquinone form porous organic polymer with "protic salt"-typed rigid skeleton linked by $-NH_2^+Cl^--$ "rivets", which offers the cornerstone for H-bonding self-assembly of the organic backbone to carbon superstructures by π−π plane stacking. The superstructures achieve ultra-stable and fast proton-coupled charge storage kinetics, giving unprecedented lifespan (1,000,000 cycles) and high energy-density for carbon (zinc) supercapacitors.

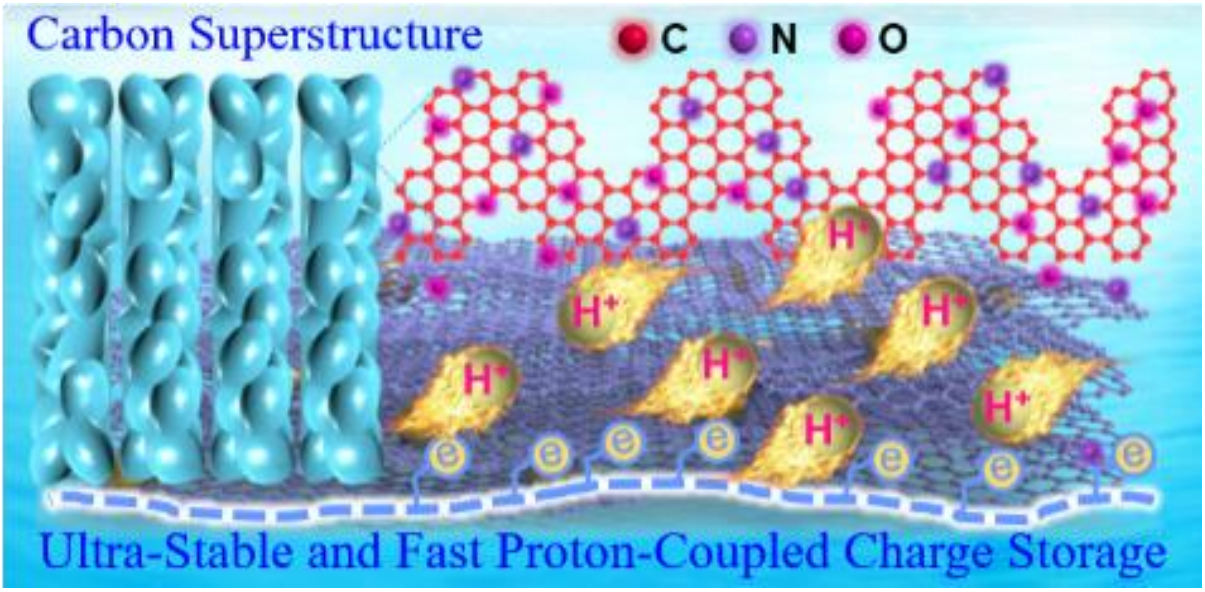

Supporting Information

Self-Assembled Carbon Superstructures Achieving Ultra-Stable and Fast Proton-Coupled Charge Storage Kinetics

Ziyang Song, Ling Miao, Laurent Ruhlmann, Yaokang Lv, Dazhang Zhu, Liangchun Li, Lihua Gan, and Mingxian Liu*

Ziyang Song, Dr. Ling Miao, Prof. Dazhang Zhu, Prof. Liangchun Li, Prof. Lihua Gan, Prof. Mingxian Liu
Shanghai Key Lab of Chemical Assessment and Sustainability, School of Chemical Science and Engineering, Tongji University, Shanghai 200092, P. R. China.
E-mail: liumx@tongji.edu.cn

Prof. Laurent Ruhlmann, Dr. Yaokang Lv
Institut de Chimie (UMR au CNRS n°7177), Université de Strasbourg, 4, rue Blaise Pascal CS 90032, F-67081 Strasbourg Cedex, France.

Dr. Yaokang Lv
College of Chemical Engineering, Zhejiang University of Technology, Hangzhou 310014, P. R. China.

Table of Contents

Section S5. Kinetics Exploration of Carbon-Based Supercapacitors.

Section S6. Electrochemistry Characterization of the Assembled Zn-Ion Device.

Section S1. Experimental Details.

1. Synthesis of Carbon Superstructure.

0.92 g (5 mmol) of 2,4,6-trichloro-1,3,5-triazine (TT) dissolved in acetonitrile (50 mL) was added into a mixture of 1.79 g (7.5 mmol) 2,6-diaminoanthraquinone (DQ) and 50 mL acetonitrile at 80 °C under stirring for 0.5−3 h. The TT-DQ polymer was collected by filtration, washing, and drying, followed by a one-step carbonization/activation using sodium cyanate as the activator (1:1, w/w) under N_2 atmosphere at 800 °C (3 °C min^{-1}) for 2 h to yield the carbon superstructures. For comparison, the carbons were also prepared under the same synthesis steps except addition of 4.2 mL triethylamine (TEA).

2. Characterization.

The sample morphologies were observed using scanning electron microscopy (SEM, Hitachi S-4800) and transmission electron microscopy (TEM, JEM-2100). Nitrogen sorption measurements were carried out using a Micromeritics apparatus (ASAP 2460) at the liquid nitrogen temperature (−196 °C). The surface area and pore size distribution were calculated using the Brunauer−Emmett−Teller (BET) equation and the nonlocal density functional theory equilibrium model. The surface chemistry was studied by an X-ray photoelectron spectrometer (XPS, AXIS Ultra DLD). Fourier-transformed infrared spectrum (FT-IR) was collected on a Thermo Nicolet NEXUS spectrometer. The material structure was characterized by X-ray diffraction (XRD, Bruker D8 advance powder diffractometer with a Cu Kα radiation source).

3. Electrochemical Evaluation.

Symmetric Supercapacitors. The working electrodes were prepared by pressing a slurry mixture containing carbon materials (80 wt%), graphite (10 wt%), and polytetrafluoroethylene (10 wt%) onto the stainless-steel sheet, and then dried at 80 °C (the mass loading of the active substance is about 10 mg cm^{-2}). The 2016 coin-type cells were assembled by stacking two same

working electrodes with a Celgard 3501 polypropylene membrane in the middle using 100 μL different electrolytes of 6 M KOH, 1 M H_2SO_4, 1 M Na_2SO_4, LiTOF (lithium trifluoromethane sulfonate in deionized water, 21 mol kg^{-1}), 1 M $TEMABF_4$/ACN (triethylmethylammonium tetrafluoroborate in deuterated acetonitrile), neat $EMIMBF_4$ (1-ethyl-3-methylimidazolium tetrafluoroborate).

The electrochemical performances were characterized on a CHI660E electrochemical workstation including cyclic voltammetry (CV), galvanostatic charge–discharge (GCD), and electrochemical impedance spectroscopy (EIS). The gravimetric capacitance (C_s) of a single electrode of the linear supercapacitors were calculated based on the following equations:

$$C_s\ (\mathrm{F\ g^{-1}}) = \frac{4 \times I \times \Delta t}{m \times \Delta V} \tag{1}$$

For a nonlinear supercapacitor, the capacitance is calculated from the integrated form:

$$\mathrm{C} = \frac{\int \mathrm{d}Q}{\int \mathrm{d}V} = \frac{\int I \mathrm{d}t}{\int \mathrm{d}V} = \frac{i\Delta t}{\Delta V} \tag{2}$$

The energy density (E) and power density (P) of the supercapacitors were calculated according to the following equations:

$$E\ (\mathrm{Wh\ kg^{-1}}) = \frac{1}{7.2 \times 4} C_s \Delta V^2 \tag{3}$$

$$P\ (\mathrm{W\ kg^{-1}}) = \frac{E}{\Delta t} \times 3600 \tag{4}$$

I (A), Δt (s), m (g), and ΔV (V) denotes charge current, discharge time, the total mass of active materials on two electrodes, and the voltage window, respectively.

Zn-Ion Hybrid Supercapacitor. Carbon//$Zn(CF_3SO_3)_2$//Zn hybrid supercapacitor was assembled in 2032 coin-type cell with the as-prepared carbon electrode as cathode, Zn foil as anode and 3 M $Zn(CF_3SO_3)_2$ as electrolyte. The specific capacity (C_m, mAh g^{-1}) and cycling performance were estimated on a LAND-CT3001A multichannel galvanostat within the voltage range of 0−1.8 V, CV and EIS tests were performed using a CHI660E electrochemical workstation.

4. DFT Calculation.

The spin-polarized DFT calculations were performed by employing Vienna Ab initio Simulation Package (VASP).[1] The projector-augmented wave (PAW) pseudopotentials[2] with a plane-wave cutoff of 520 eV and Perdew-Burke-Ernzerhof (PBE) function[3] of the generalized gradient approximation (GGA) were adopted to model the electron exchange-correlation interactions. The convergence criterion for the structural optimizations was set to be 1×10^{-5} eV, and all atomic structures were allowed to be relaxed until the residual forces on each atom dropped below 0.02 eV $Å^{-1}$. The geometric optimization was performed by the 3×3×1 Monkhorst−Pack k-point mesh. A supercell of graphene containing 6×6 unit cells with a vacuum region of 20 Å thickness was created to ensure negligible interaction between slabs for describing the N/O codoped carbon systems. The adsorption energy was calculated based on the form:

$$E_{ads} = E_{H/carbon} - E_{carbon} - E_{H} \quad (5)$$

where $E_{H/carbon}$, E_{carbon}, and E_{H} denote energies of carbon systems with and without H adsorption, and the energy of single H atom in bulk structure, respectively. The more negative the adsorption energy values signify the stronger the H adsorption strength on the carbon systems.

To describe the bonding nature of H adsorbed on doped carbon systems and charge transfer between them in detail, the charge density differences of H absorbed on the constructed carbon structures were calculated by subtracting the charge densities of the H atom and carbon substrates from the corresponding compounds.

$$\Delta\rho = \rho_{H/carbon} - \rho_{carbon} - \rho_{H} \quad (6)$$

The barriers of H ion diffusion on pyrrole-N graphene systems were calculated using the climbing image nudged elastic band (CI-NEB) approach.[4] Bader charge calculations were performed to analyze the charge transfer and the interaction intensity between H and N/O-substituted active sites.

References

S1. G. Kresse, J. Furthmüller, Efficient iterative schemes for ab initio total-energy calculations using a plane-wave basis set, *Phys. Rev. B* **1996**, *54*, 11169−11186.

S2. P. E. Blochl, Projector augmented-wave method. *Phys. Rev. B* **1994**, *50*, 17953−17979.

S3. J. P. Perdew, K. Burke, M. Ernzerhof, Generalized gradient approximation made simple. *Phys. Rev. Lett.* **1996**, *77*, 3865−3868.

S4. G. Henkelman, B. P. Uberuaga, H. Jónsson, A climbing image nudged elastic band method for finding saddle points and minimum energy paths. *J. Chem. Phys.* **2000**, *113*, 9901−9904.

Section S2. Structural Characterization of −$NH_2^+Cl^-$− Linked TT-DQ Skeletons.

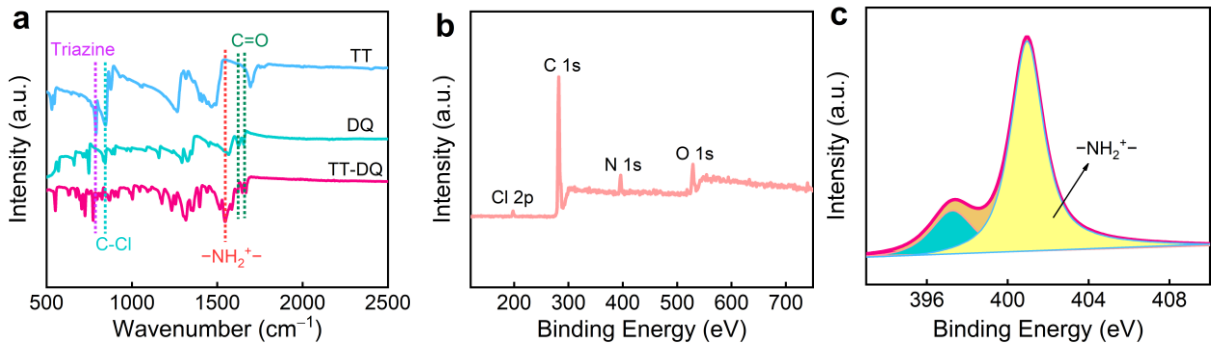

Figure S1. (a) FT-IR spectra, (b) wide-scan XPS spectra and (c) high-resolution spectra of N 1s for TT-DQ skeleton at the polymerization time of 1 min.

Notes to Figure S1a: The triazine ring vibration of TT moves from 791 cm^{-1} to 769 cm^{-1} in TT-DQ, while the C=O stretching vibration of DQ at 1623 and 1658 cm^{-1} is shifted to 1646 and 1671 cm^{-1} in TT-DQ. A shift of the triazine ring vibration of TT to a lower frequency and the C=O stretching vibration of DQ to a higher frequency confirm the existence of hydrogen-bonding interactions of N−H···O and N−H···N between adjacent polymer networks.

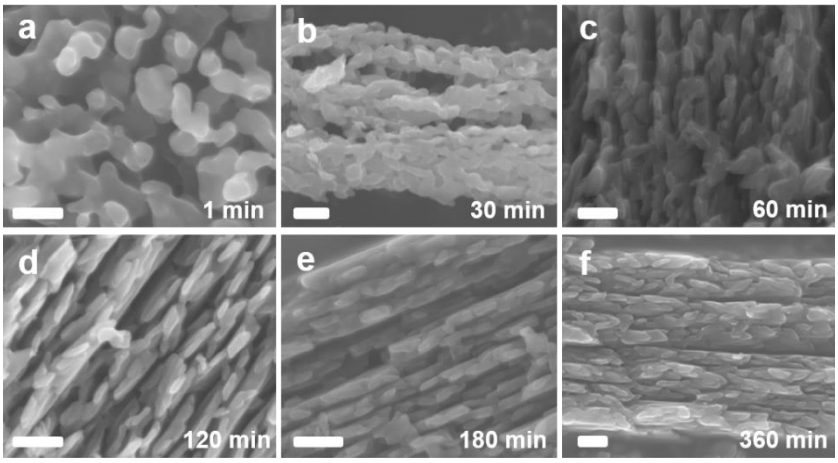

Figure S2. Morphological evolution of TT-DQ polymers at different polymerization times.

Table S1. Comparison of TEA dosage (mM) and pH values of the reaction solutions, formed linkers, skeleton and morphology of TT-DQ polymers, surface areas (S_{BET}) and heteroatom contents of the resultant carbons.

TEA	pH	Linker	Skeleton	Morphology	S_{BET} (m^2 g^{-1})	N/O (wt.%)
0	6.84	−$NH_2^+Cl^-$−	Rigidity	Superstructure	158	10.22/5.04
300	8.01	−NH−	Flexibility	Disordered structure	8	5.47/6.80

Section S3. Physicochemical Analysis of the Carbon Superstructures.

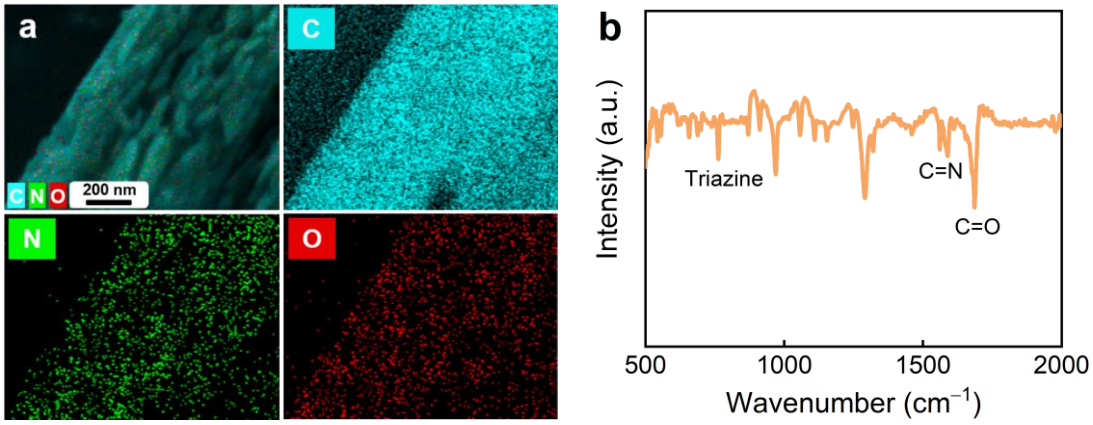

Figure S3. (a) Elemental mapping images of C, N and O and (b) FI-IR spectra for carbon superstructures.

Table S2. S_{BET}, heteroatom contents, relative contents of N-6/N-5 and O-1 species, the contents of effective heteroatomic species (EHS) and electrochemical capacitances (C_s) of carbon superstructures based on TT-DQ polymers at different polymerization times.

Time (min)	S_{BET} ($m^2\ g^{-1}$)	N (wt.%)	O (wt.%)	N-6+N-5 (%)	O-1 (%)	EHS[a] (wt.%)	C_m ($F\ g^{-1}$)
1	1249	6.49	6.92	55.5	34.1	5.96	302
30	1466	7.37	7.64	65.3	35.2	7.68	329
60	1662	8.07	7.01	67.8	34.8	7.91	369
120	1668	8.14	7.28	66.5	40.3	8.35	415
180	1993	10.22	5.04	71.9	69.1	10.83	468
360	1913	7.99	7.81	66.6	43.4	8.71	458

[a]EHS (wt.%) = (N-6 + N-5) × N% + O-1 × O%.

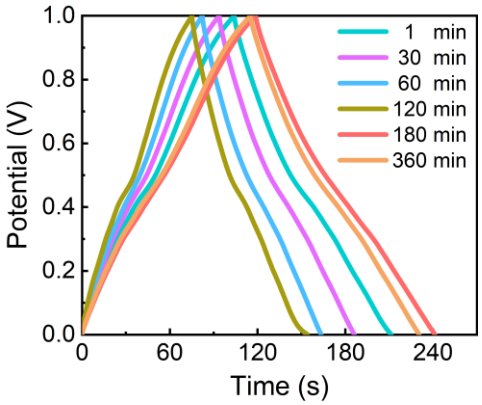

Figure S4. GCD profiles of the assembled supercapacitors based on carbon superstructures derived from different polymerization times.

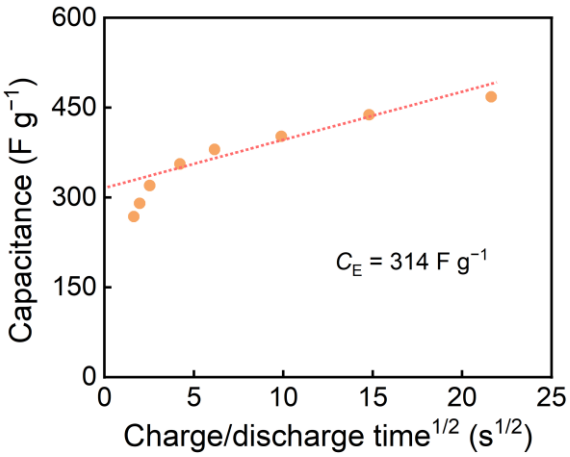

Figure S5. The capacitance *vs.* square root of half-cycle time.

Notes: We calculated the respective capacitance contribution from electrical double layer capacitances (C_E) and pseudocapacitance (C_P) based on the following Equation:

$$C = k_1 + k_2 v^{-1/2} \quad (7)$$

where the capacitance C includes a rate-independent component k_1 (generally related to C_E) and a diffusion-limited part determined by the scan rate, $v = T^{-1}$. In the GCD test, T is the discharge time. C_E can be obtained from the intersection of fitting line and vertical axis. From GCD test, the C_E values is 314 F g^{-1}, thus the C_P contribution is 154 F g^{-1} (32.9% of the total electrode capacitance).

Section S4. Electrochemical Charge Storage of Carbon-Based Supercapacitors.

The Dunn's method was employed to quantify the capacitance contribution from fast-kinetic processes (including electrical double-layer capacitive processes and surface rapid redox reactions) and slow-kinetic processes (redox reactions that are diffusion-controlled). The charge-storage kinetic information can be collected by analyzing the relationship between current (i) and the scan rate (v), which can be expressed as the following:

$$i = k_1 v + k_2 v^{1/2} \quad (8)$$

where the k_1 and k_2 are constants, $k_1 v$ accounts for the current density contributed from fast-kinetic process. The second term $k_2 v^{1/2}$ corresponds to the current density associated with slow-kinetic (or diffusion-limited) process. Dividing $v^{1/2}$ on both sides of the equation yields:

$$i/v^{1/2} = k_1 v^{1/2} + k_2 \quad (9)$$

Therefore, $i/v^{1/2}$ and $v^{1/2}$ are expected to generate a linear relationship, the capacitance contribution from fast/slow kinetics can be differentiated by linear fitting. The slope corresponds to k_1 and the y-intercept equals k_2. By repeating the above steps for other potentials and scan rates, the respective capacitance contribution from fast and slow reactions can be quantitatively mapped out. The ratio of fast capacitance to total capacitance equals the ratio of the area of the marked region to the area of the total CV region.

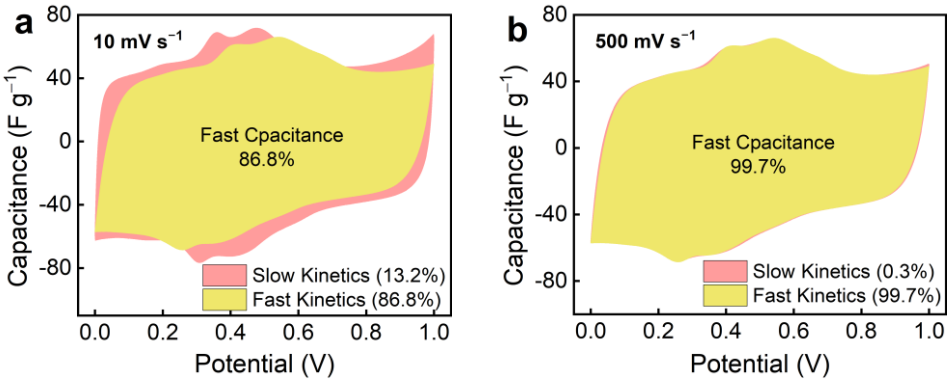

Figure S6. Capacitance contribution from fast and slow kinetics at (a) 10 and (b) 500 mV s^{-1}.

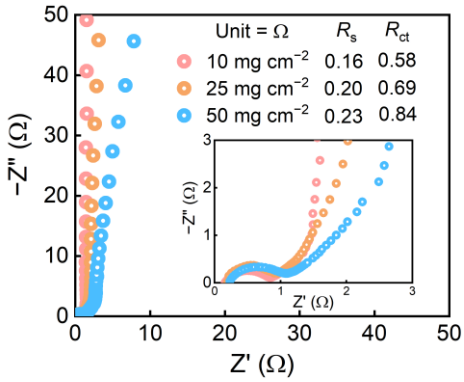

Figure S7. EIS spectra of the devices with various mass loadings of active materials.

Notes: The close-to-vertical lines at low frequency region exhibit good ion diffusion and desirable capacitive property, and the intersection points on the horizontal axis as well as the semicircles in the high-range frequency domain correspond to the equivalent series resistance (R_s) and charge-transfer resistance (R_{ct}). Apparently, the devices possess low R_s values of 0.16−0.23 Ω and R_{ct} values of 0.58−0.84 Ω. In addition, in the mid-frequency Warburg region, the knee frequency (f) describes the maximum frequency at the phase angle of −45° where the capacitive behavior is dominant. The higher f is, the faster the supercapacitor energy can be stored and released. The corresponding knee frequency is calculated to 6.67, 2.13, and 1.20 Hz. The results reveal the good kinetics and high-rate capability of the electrode in acidic electrolyte. Generally, the charge storage capability of the carbon superstructure device decreases with increasing mass loadings owing to that the elongated ion/electron transport routes under higher mass loadings lead to relatively sluggish electrochemically reaction kinetics and blocked supercapacitive activity. R_s and R_{ct} slightly change even at 50 mg cm^{-2}, suggesting robust electrolyte reaction kinetics.

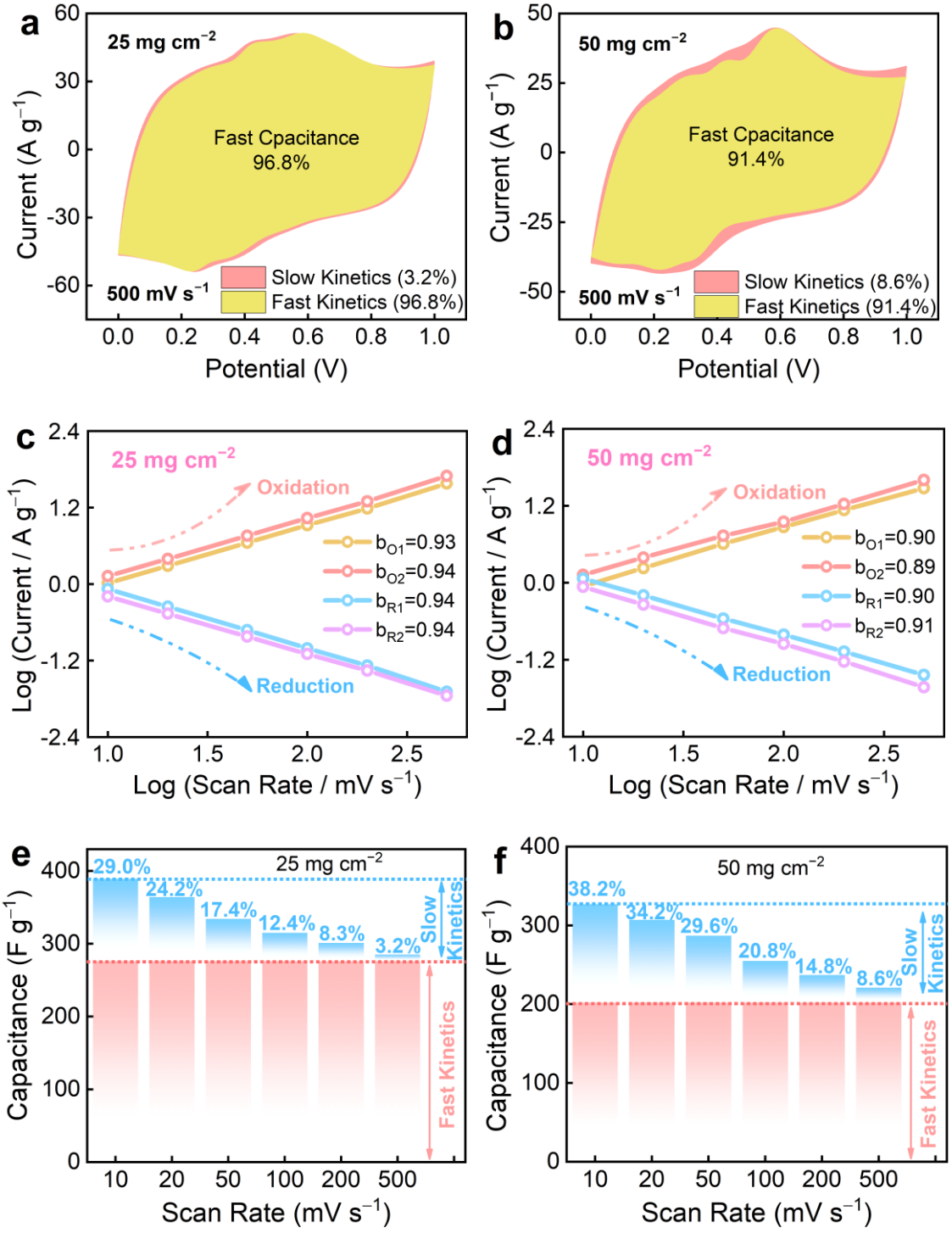

Figure S8. Ultrarapid charge-storage kinetics of the assembled supercapacitors under two mass loadings of 25 and 50 mg cm^{-2} in H_2SO_4 electrolyte. (a, b) Capacitance contribution. (c, d) The fitting plots between log*i* and log*v*. (e, f) The electrode capacitance contribution from fast and slow kinetic responses.

Table S3. The capacitances fitted by the area of CV profiles at different scan rates, the rate performances, the range of *b* values, and the capacitance originated from fast-kinetic process of the carbon electrode with different mass loadings of active materials in H_2SO_4 electrolyte.

Mass loading ($mg\ cm^{-2}$)	Scan rate ($mV\ s^{-1}$)						Rate (%)	*b* value	Fast capacitance ($F\ g^{-1}$)
	10	20	50	100	200	500			
10	423	408	398	380	373	368	87.2	0.98~0.99	367
25	389	364	334	315	301	285	71.1	0.93~0.94	276
50	327	307	287	255	237	221	67.6	0.89~0.91	202

Table S4. Supercapacitive performances of the carbon electrode at different current densities under various mass loadings of active materials in H_2SO_4 electrolyte.

Mass loading ($mg\ cm^{-2}$)	Current density ($A\ g^{-1}$)								Rate (%)
	1	2	5	10	20	50	75	100	
10	468	438	402	380	356	320	290	269	57.5%
25	418	406	376	332	308	268	236	216	51.7%
50	350	334	315	289	262	228	192	162	46.3%

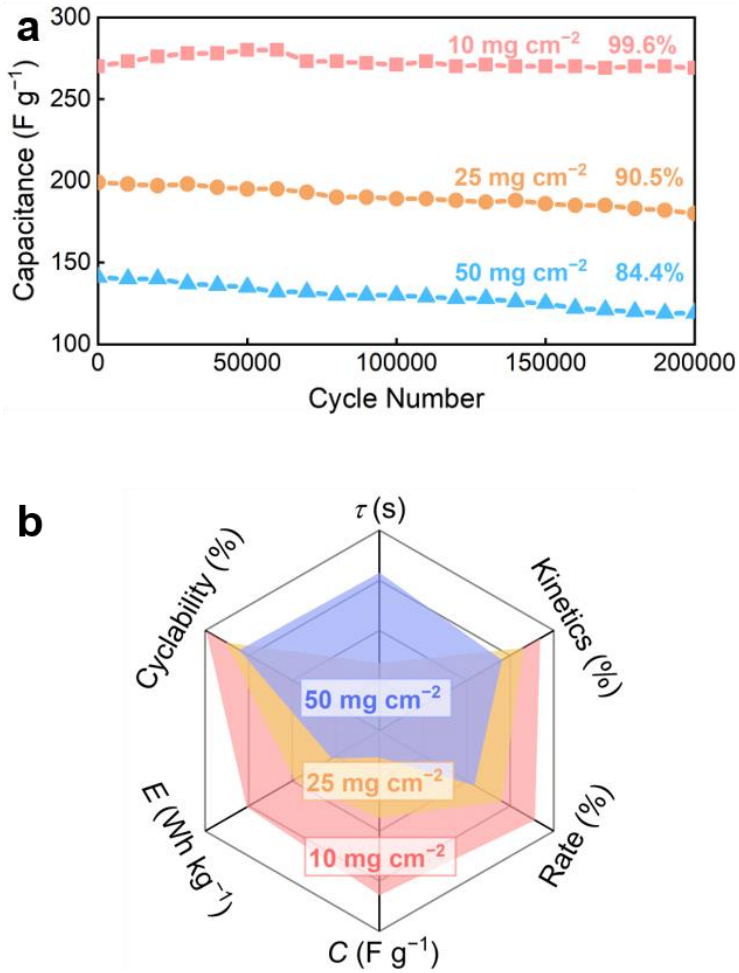

Figure S9. (a) Long-term cycling stability of carbon supercapacitors at 100 A g^{-1} over 200,000 cycles, and (b) the contrastive radar chart of the six figure-of-merits of carbon supercapacitors with different mass loadings of active materials.

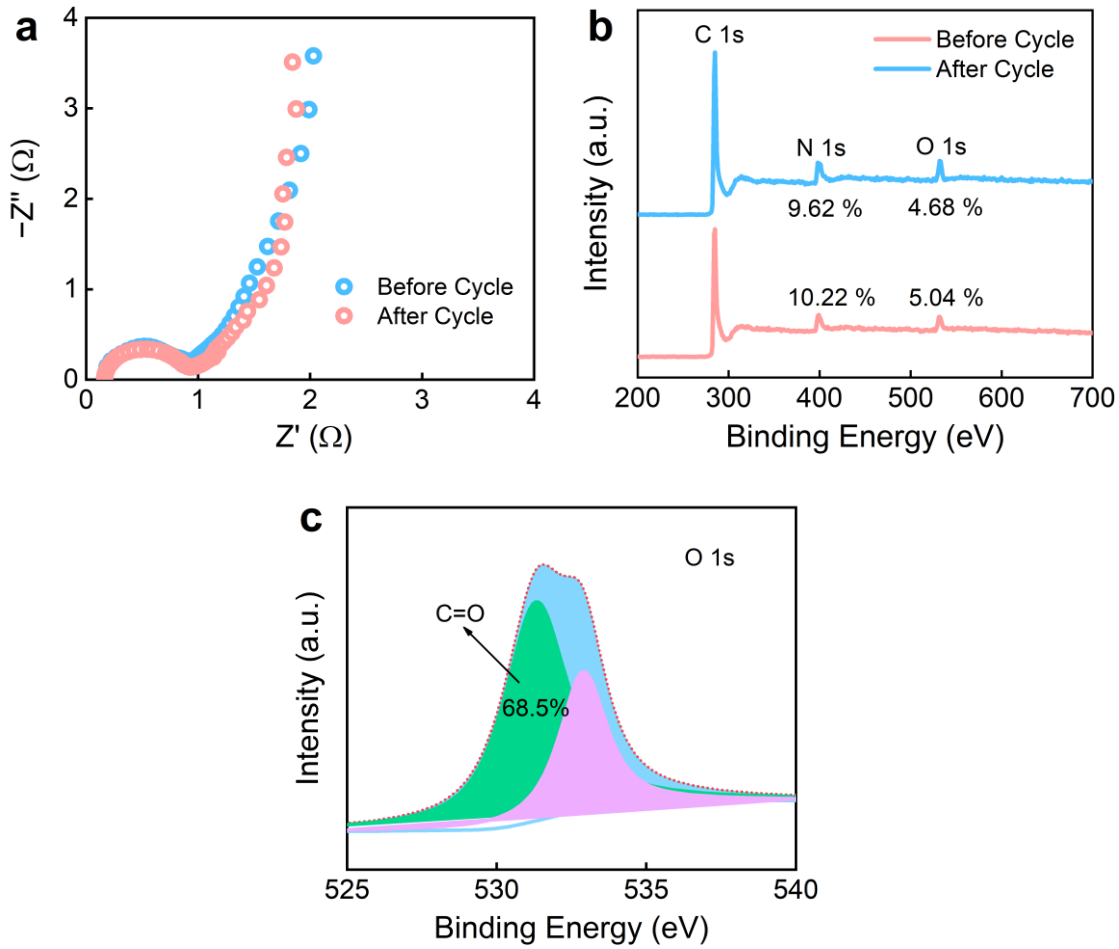

Figure S10. (a) Nyquist plots, (b) XPS spectra and (c) high-resolution O 1s of the carbon electrode with 10 mg cm^{-2} after long-term cycling test.

Table S5. Comparison of C_s, mass loading of active materials and cycle stability of reported carbon electrodes for supercapacitors in the recent literatures.

Materials	C_s F g^{-1}@A g^{-1}	Mass Loading (mg cm^{-2})	Lifespan %@Cycle@mV s^{-1} or A g^{-1}	Ref.
MXene/graphene	383@1 294@10	N/A	97@30,000@200 mV s^{-1}	S5
Hollow spheres	251@0.5 191@15	N/A	140@8,000@3 A g^{-1}	S6
Doped carbons	348@0.5 123@80	2.5	92@35,000@20 A g^{-1}	S7
Ordered carbon	236@0.5 171@100	1.0	105@10,000@50 mV s^{-1}	S8
COF/aerogel	269@0.5 222@10	1.0	96@5,000@8 A g^{-1}	S9
Porous carbon	231@0.1 150@10	1.8~2.7	123@80,000@10 A g^{-1}	S10
Carbon nanofiber	279@0.5 165@20	N/A	122@10,000@5 A g^{-1}	S11
Porous carbon	357@1 110@80	1.0~4.0	98@60,000@10 A g^{-1}	S12
Carbon microspheres	301@0.2 210@5	8.0	100@5,000@5 A g^{-1}	S13
Carbon fiber textile	220@0.5 80@50	N/A	100@10,000@5 mV s^{-1}	S14
Carbon aerogels	300@0.5 221@10	1.5	92@5,000@2 A g^{-1}	S15
Porous carbon	202@0.5 141@40	9.0~11.0	100@8,000@5 A g^{-1}	S16
Carbon nanosheets	280@0.5 228@100	N/A	103@10,000@6 A g^{-1}	S17
Biomass carbon	307@0.5 181@30	N/A	96.5@10,000@5 A g^{-1}	S18
Carbon sheets	208@0.2 106@100	N/A	99@20,000@1 V s^{-1}	S19
Carbon Superstructures	**468@1 269@100**	**10.0**	**103.7@60,000@100 A g^{-1} 93.1@1,000,000@100 A g^{-1}**	**This Work**

References

S5. X. Yang, Q. Wang, K. Zhu, K. Ye, G. Wang, D. Cao, J. Yan, *Adv. Funct. Mater.* **2021**, *31*, 2101087.

S6. Y.-Y. Liu, X.-C. Li, S. Wang, T. Cheng, H. Yang, C. Liu, Y. Gong, W.-Y. Lai, W. Huang, *Nat. Commun*. **2020**, *11*, 5561.

S7. C. Cui, Y. Gao, J. Li, C. Yang, M. Liu, H. Jin, Z. Xia, L. Dai, Y. Lei, J. Wang, S. Wang, *Angew. Chem. Int. Ed.* **2020**, *132*, 2–8.

S8. Q. Li, Z. Dai, J. Wu, W. Liu, T. Di, R. Jiang, X. Zheng, W. Wang, X. Ji, P. Li, Z. Xu, X. Qu, Z. Xu, J. Zhou, *Adv. Energy Mater.* **2020**, *10*, 1903750.

S9. C. Li, J. Yang, P. Pachfule, S. Li, M. Y. Ye, J. Schmidt, A. Thomas, *Nat. Commun.* **2020**, *11*, 4712.

S10. F. Hu, T. Zhang, J. Wang, S. Li, C. Liu, C. Song, W. Shao, S. Liu, X. Jian, *Nano Energy* **2020**, *74*, 104789.

S11. Y. Yang, Y.-x. Liu, Y. Li, B.-w. Deng, B. Yin, M.-b. Yang, *J. Mater. Chem. A* **2020**, *8*, 17257−17265.

S12. H. Jin, X. Feng, J. Li, M. Li, Y. Xia, Y. Yuan, C. Yang, B. Dai, Z. Lin, J. Wang, J. Lu, S. Wang, *Angew. Chem. Int. Ed.* **2019**, *131*, 2419−2423.

S13. T. Wang, Y. Sun, L. Zhang, K. Li, Y. Yi, S. Song, M. Li, Z. A. Qiao, S. Dai, *Adv. Mater.* **2019**, *31*, 1807876.

S14. Q. Li, J. Wang, C. Liu, S. M. Fakhrhoseini, D. Liu, L. Zhang, W. Lei, M. Naebe, *Adv. Sci.* **2019**, *6*, 1900762.

S15. H. Li, J. Li, A. Thomas, Y. Liao, *Adv. Funct. Mater.* **2019**, *29*, 1904785.

S16. M. Sevilla, N. Diez, G. A. Ferrero, A. B. Fuertes, *Energy Storage Mater.* **2019**, *18*, 356−365.

S17. J. Yu, C. Yu, W. Guo, Z. Wang, S. Li, J. Chang, X. Tan, Y. Ding, M. Zhang, L. Yang, Y. Xie, R. Fu, J. Qiu, *Nano Energy* **2019**, *64*, 103921.

S18. C. Li, W. Wu, P. Wang, W. Zhou, J. Wang, Y. Chen, L. Fu, Y. Zhu, Y. Wu, W. Huang, *Adv. Sci.* **2019**, *6*, 1801665.

S19. X. Xi, D. Wu, L. Han, Y. Yu, Y. Su, W. Tang, R. Liu, *ACS Nano* **2018**, *12*, 5436−5444.

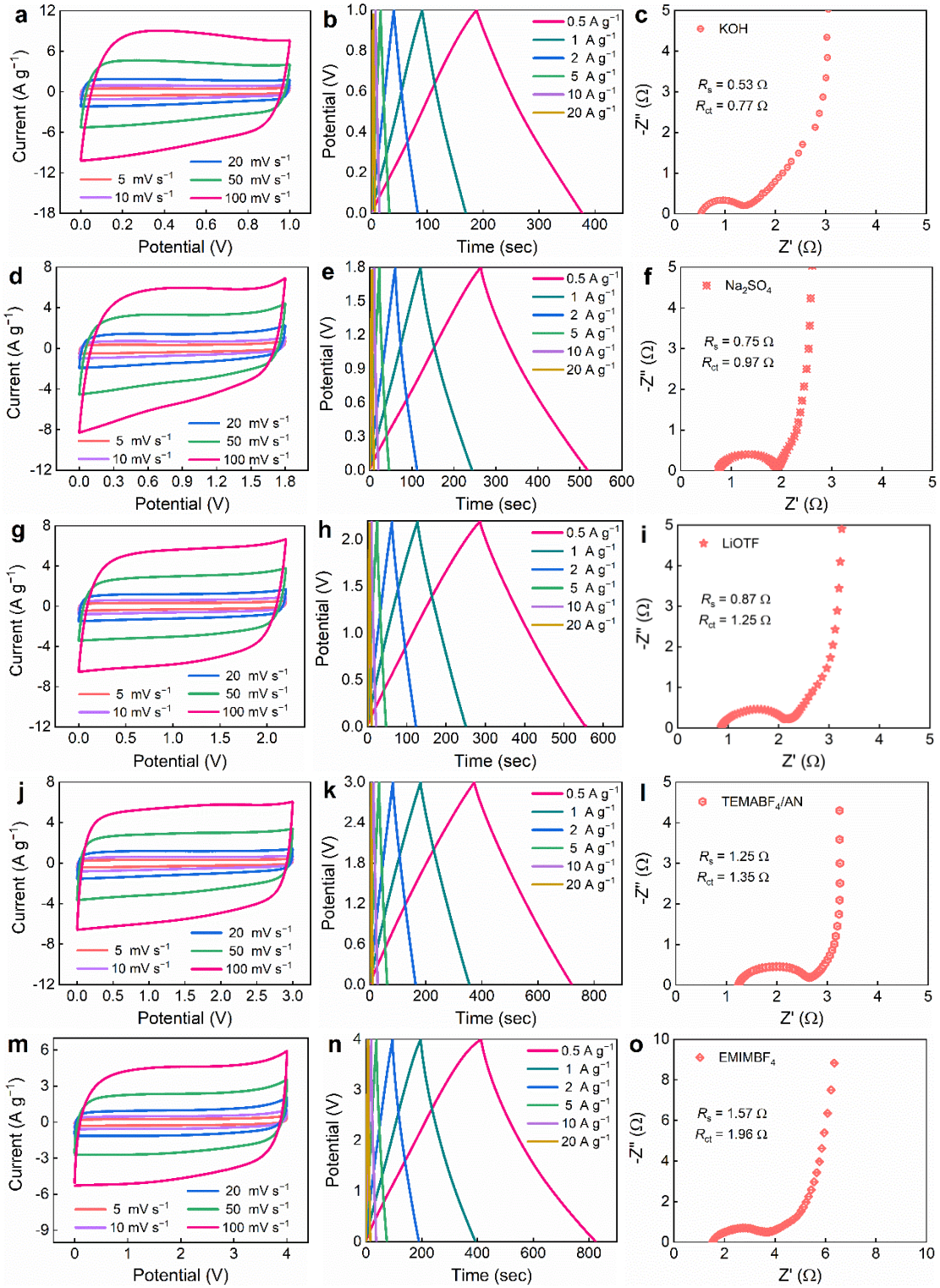

Figure S11. Electrochemical performances of the assembled carbon-based supercapacitors using different electrolytes: (a–c) 6 M KOH; (d–f) 1 M Na_2SO_4; (g–i) 21 m LiOTF; (j–l) 1 M TEMABF$_4$/AN; (m–o) EMIMBF$_4$.

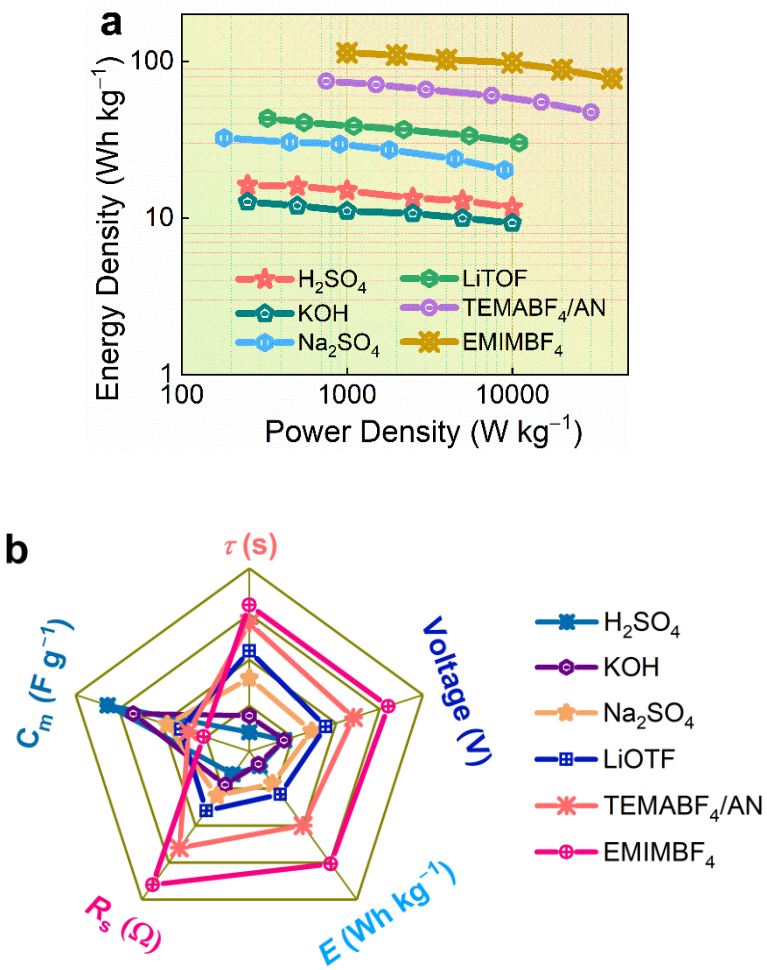

Figure S12. Comparison of electrochemical properties in different electrolytes. (a) Ragone plots and (b) radar chart of the five figure-of-merit for carbon-based devices.

Section S5. Kinetics Exploration of Carbon-Based Supercapacitors.

The electron transport and ion diffusion resistivity were analyzed with EIS based on the following forms:

$$\tau = \frac{1}{f} \tag{10}$$

$$Z' = \sigma\omega^{-0.5} + R_s + R_{ct} \tag{11}$$

$$D = \frac{R^2T^2}{2A^2C^2n^4F^4\sigma^2} \tag{12}$$

where τ: relaxation time constant (s);

f: knee frequency (Hz);

Z': real part of impedance (Ω);

ω: angle frequency (rad s^{-1});

σ: diffusion resistance (Ω $s^{-0.5}$);

R_s: ohmic resistance between the electrode and electrolyte (Ω);

R_{ct}: charge transfer resistance (Ω);

n: electron transfer numbers per molecule during electron reaction;

D: ion diffusion coefficient (cm^2 s^{-1});

A: surface area of electrode (cm^2);

R: gas constant (8.314 J mol^{-1} K^{-1});

T: Kelvin temperature (293.15 K);

C: molar concentration of electrolyte (mol L^{-1});

F: Faraday constant (96485 C mol^{-1}).

Table S6. Calculated ion resistance parameters.

State	Voltage (V)	R_s (Ω)	R_{ct} (Ω)	σ (Ω $s^{-0.5}$)	D_{H^+} (cm^2 s^{-1}) × 10^{-8}
Discharge	1.0	0.31	0.81	0.96	1.23
	0.8	0.23	0.73	0.87	1.50
	0.6	0.21	0.67	0.83	1.65
	0.4	0.20	0.65	0.79	1.82
	0.2	0.19	0.58	0.74	2.07
	0	0.18	0.42	0.64	2.77
Charge	0.2	0.19	0.59	0.76	1.97
	0.4	0.22	0.60	0.82	1.69
	0.6	0.23	0.65	0.88	1.47
	0.8	0.25	0.67	0.92	1.34
	1.0	0.29	0.84	0.98	1.18

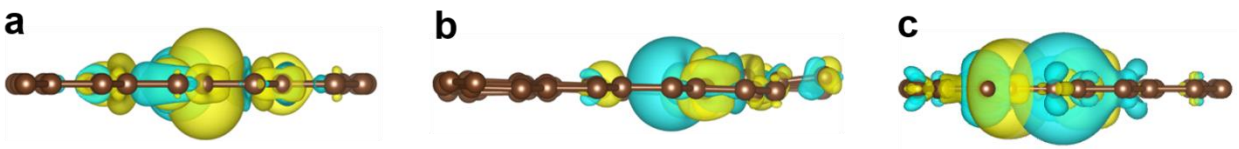

Figure S13. Side views of the electron density difference for one H ion adsorbed in carbon skeleton.

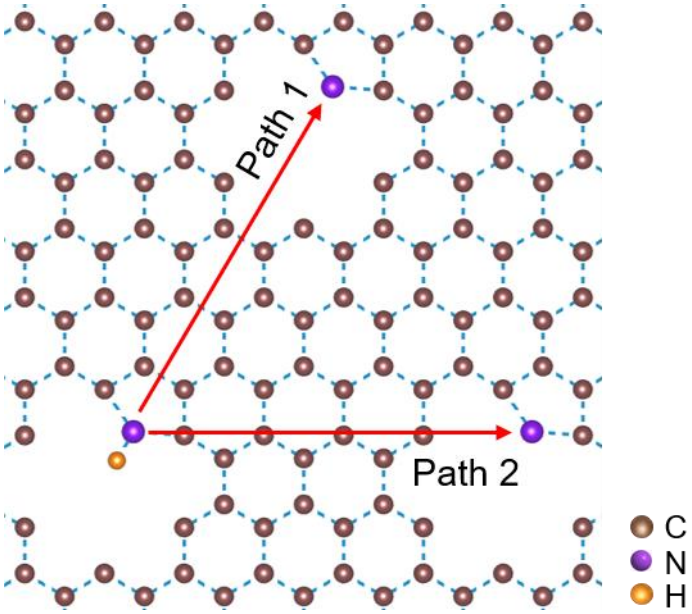

Figure S14. The diffusion paths of H ions in different models.

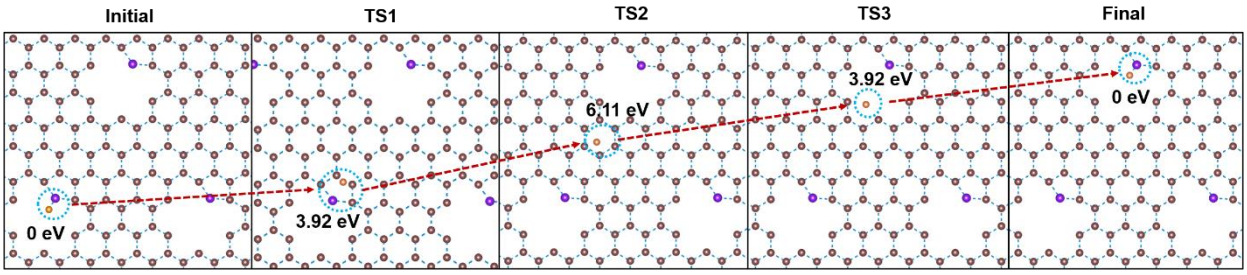

Figure S15. Top view of H ion diffusion in N-5 doping structure (path 1) and the corresponding diffusion barrier energies at various states.

Section S6. Electrochemistry Characterization of the Assembled Zn-Ion Device.

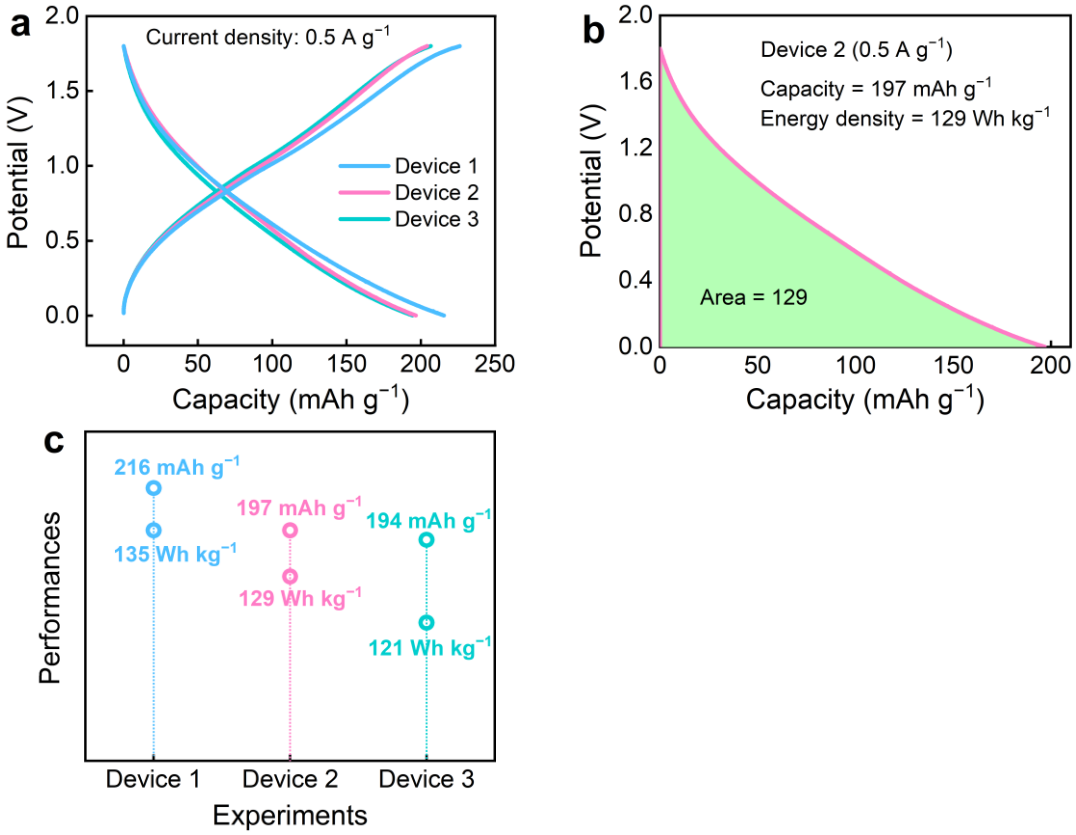

Figure S16. Repeated electrochemical experiments on three identical assembled Zn-ion devices: (a) GCD curves at 0.5 A g^{-1}, (b) the capacity and energy density of the device 2 calculated by the integral area of the GCD curve at 0.5 A g^{-1}, and (c) comparison of electrochemical performance of three devices.

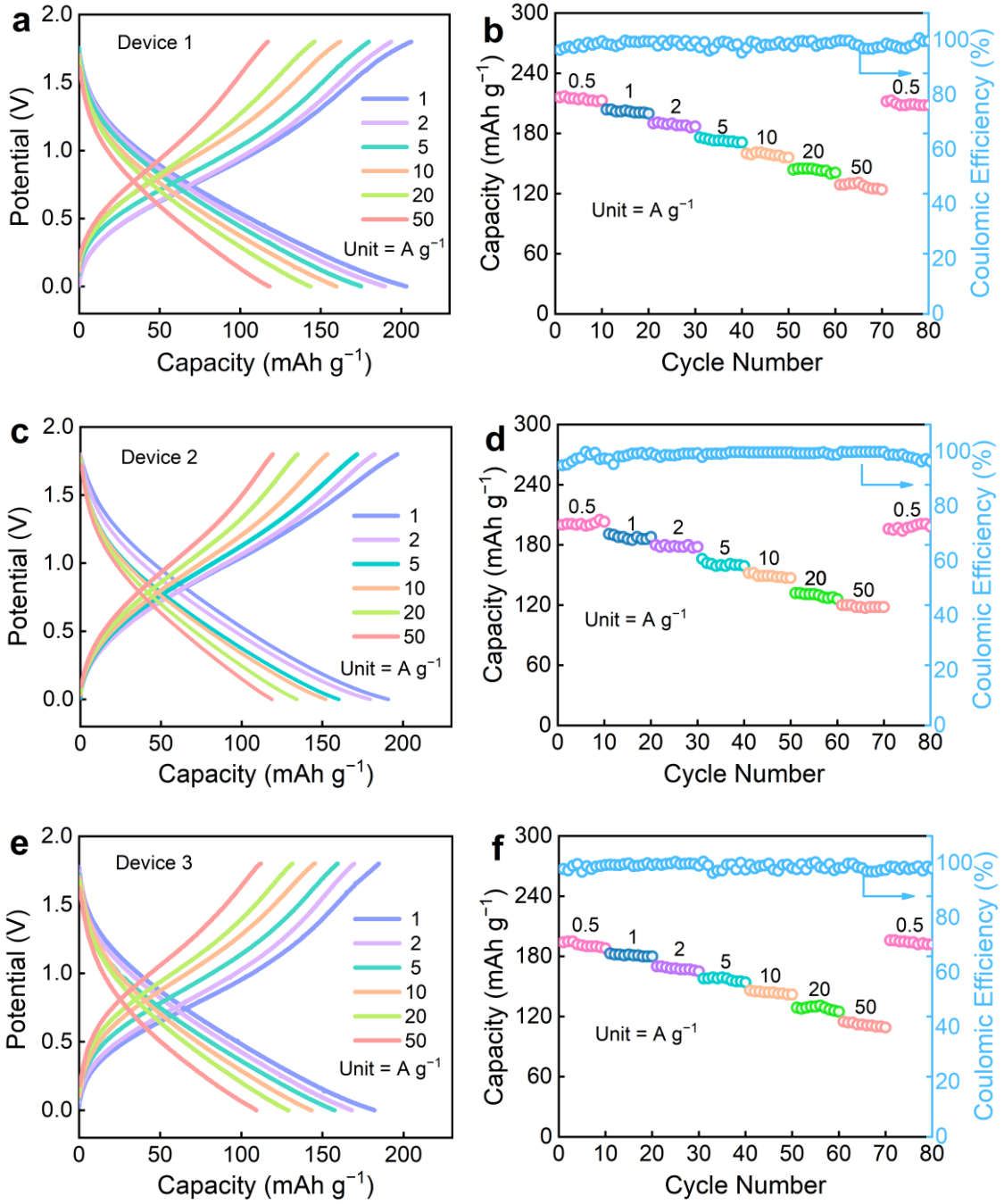

Figure S17. Repeated electrochemical experiments on three identical assembled Zn-ion devices: (a, c, e) GCD curves and (b, d, f) rate performances.

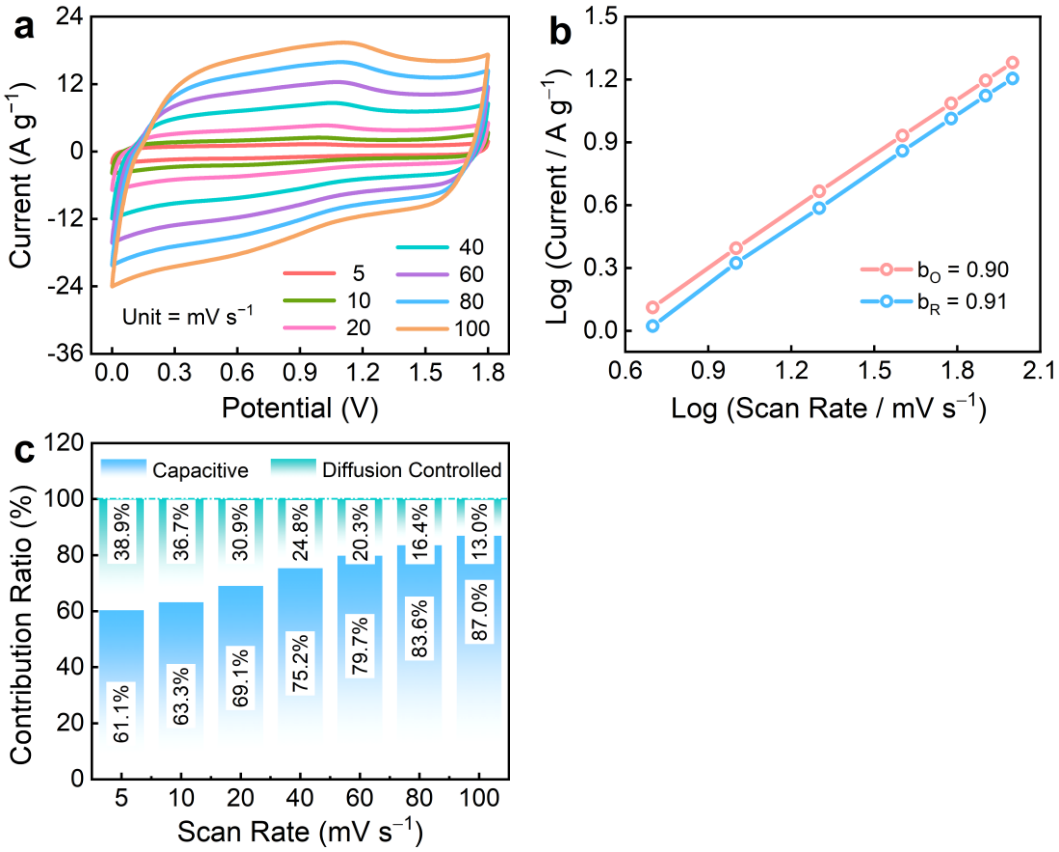

Figure S18. Investigation of the capacitive effect and diffusion-controlled energy storage behaviors of the device 2: (a) CV curves. (b) The fitting plots between log*i* and log*v* at the anodic peaks (b_O) and the cathodic peaks (b_R). (c) Normalized capacity contribution at different scan rates.

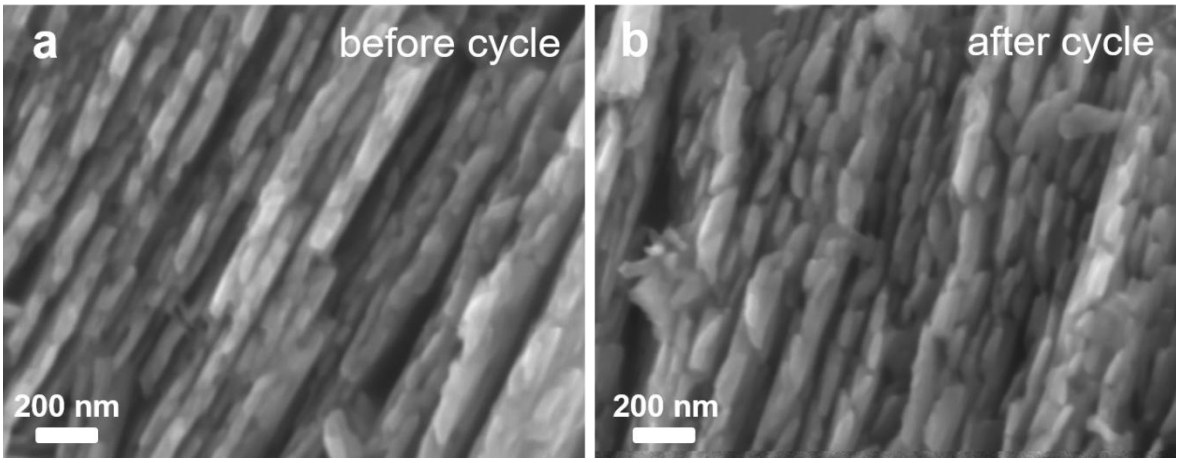

Figure S19. SEM images of the carbon cathode in Zn-ion hybrid device (a) before and (b) after 200,000 cycles.

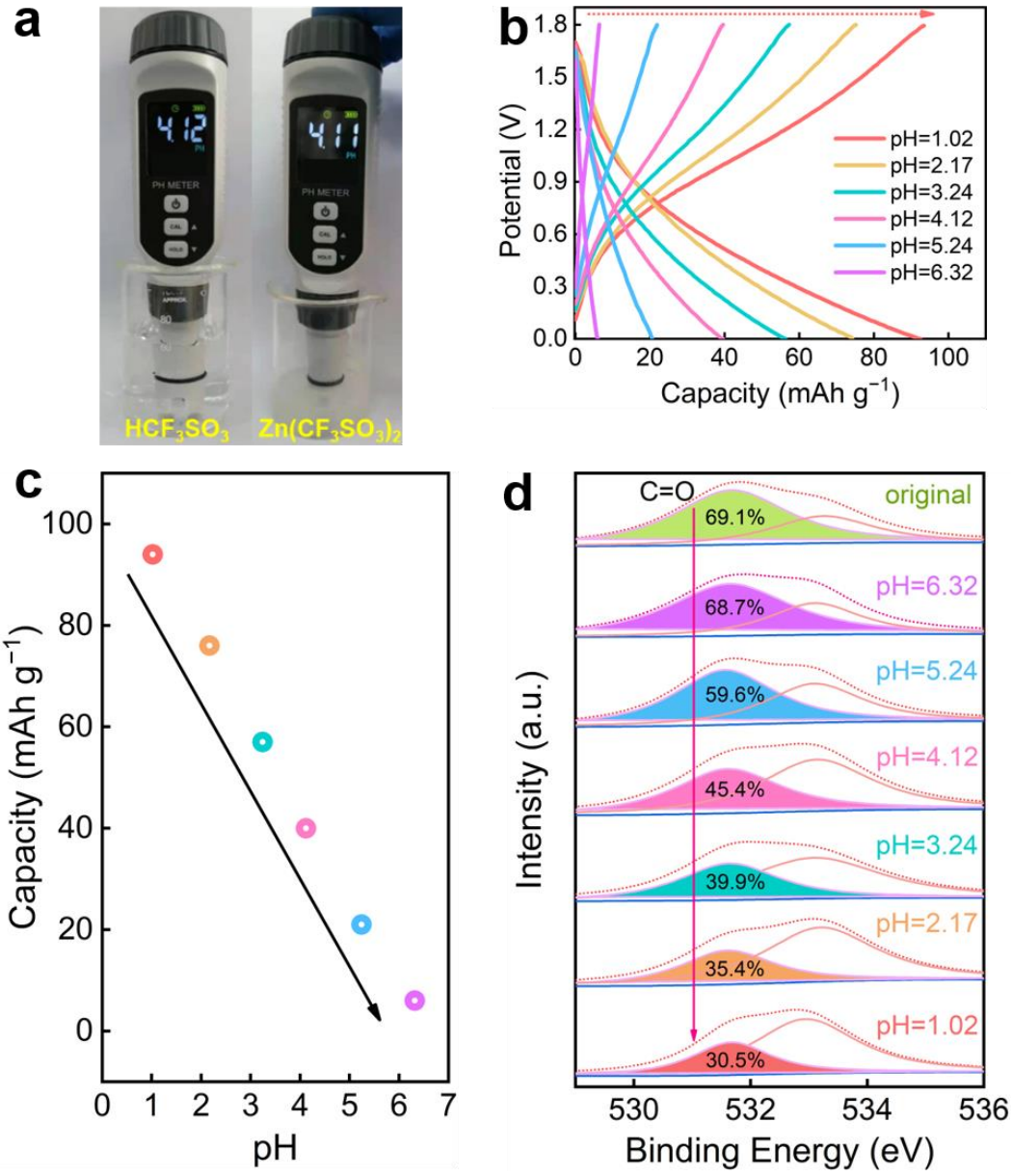

Figure S20. (a) pH values of 3 M $Zn(CF_3SO_3)_2$ and HCF_3SO_3, (b) GCD curve at 0.5 A g^{-1}, and (c) relationship between capacities of the carbon-based Zn-ion device and the pH values of HCF_3SO_3 electrolytes. (d) Ex situ high-resolution O 1s XPS spectra of the carbon cathodes using HCF_3SO_3 electrolytes with different pH values at the discharging state of 0 V.

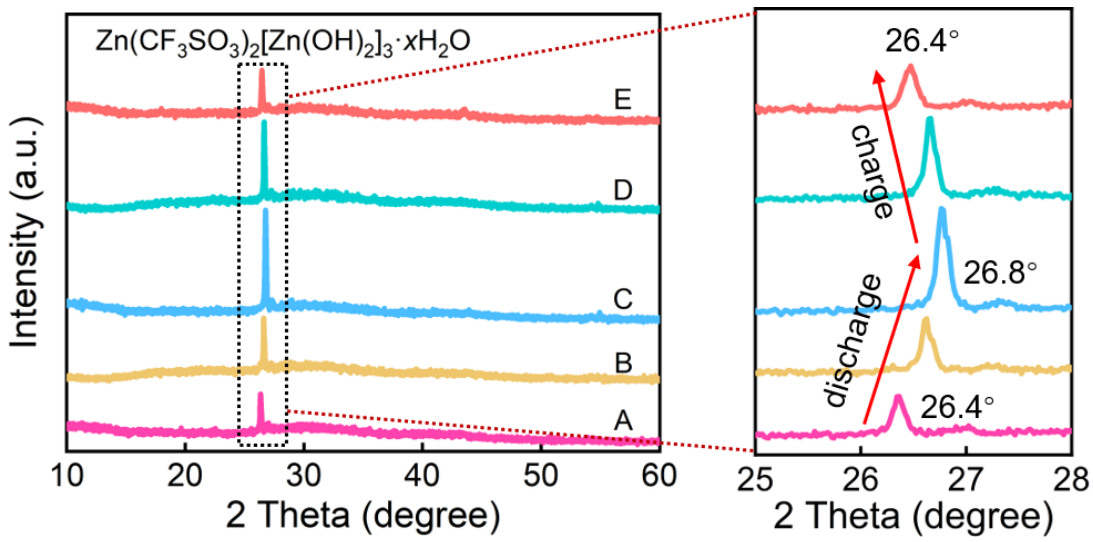

Figure S21. XRD patterns of carbon superstructure cathode at different charge/discharge states.

Notes: The co-participation of H^+ and Zn^{2+} in the cathode is also verified by XRD and element mapping. The characteristic peak positioned at ~26.4° is observed at different voltages, which can be credited to the formation of typical $Zn(CF_3SO_3)_2[Zn(OH)_2]_3{\cdot}xH_2O$ phase on the cathode surface during the electrochemistry reactions. The product of $Zn(CF_3SO_3)_2[Zn(OH)_2]_3{\cdot}xH_2O$ comes from the reaction of OH^- with $Zn(CF_3SO_3)_2$ and H_2O, while H^+ in aqueous electrolyte diffuse into carbon cathode to interact with C=O. With continuous discharging, the peak intensity gradually increases, together with the peak position shifting to a higher angle. Following the charge process, the peak feature undergoes a reverse variation trend.

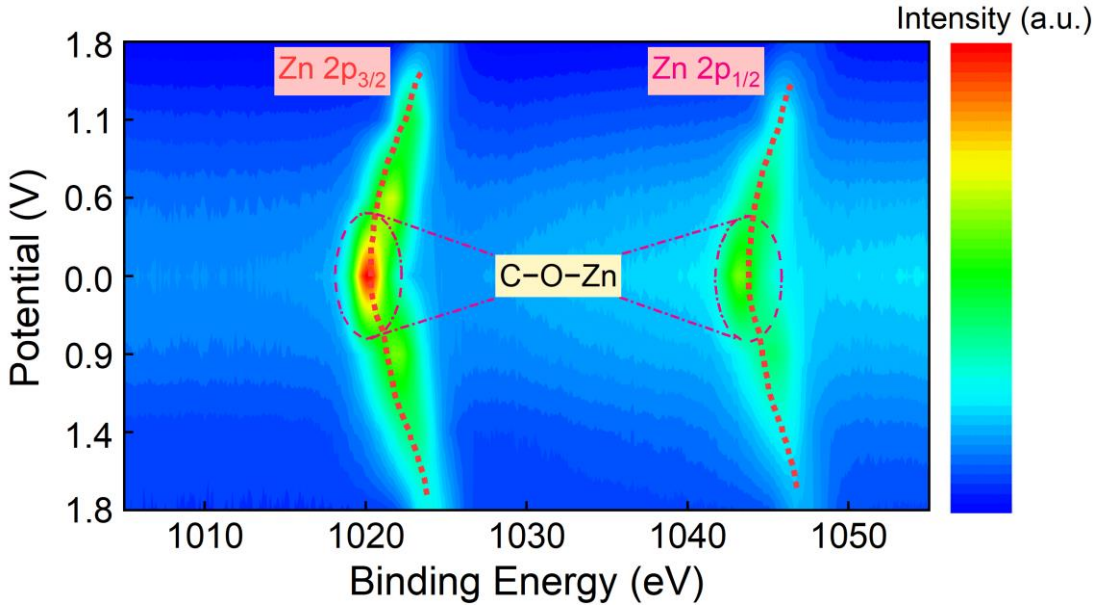

Figure S22. Ex-situ XPS spectra of Zn 2p.

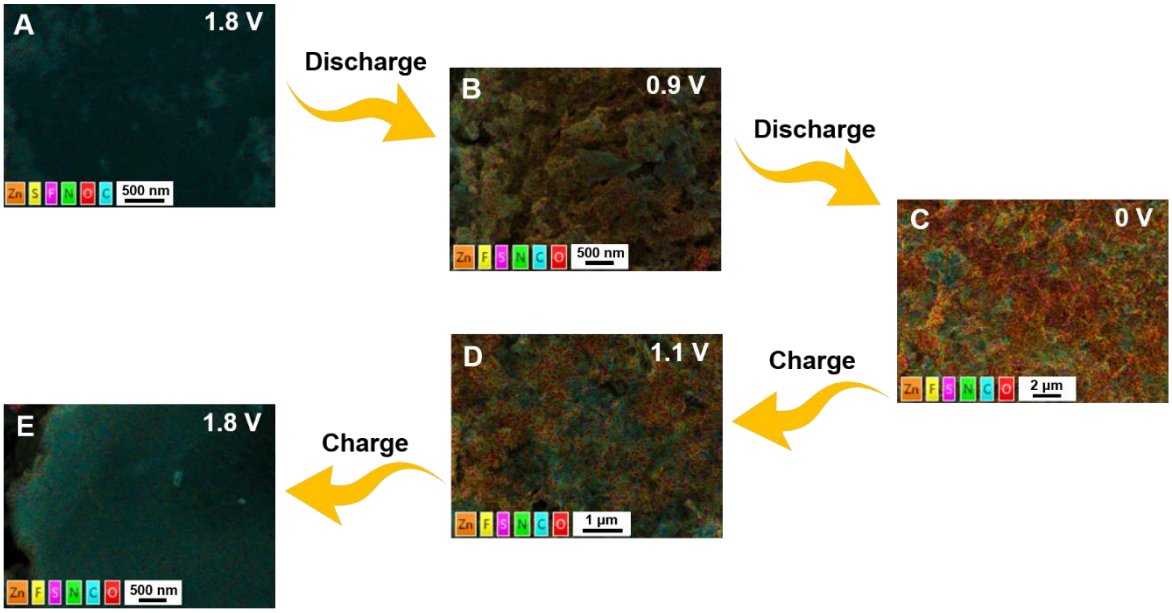

Figure S23. Elemental mapping images of carbon cathode at five representative discharging/charging moments (A, B, C, D, and E).

Table S7. X-ray electron diffraction spectroscopy data of carbon cathode corresponding to various stages of the discharging/charging courses shown in **Figure S23**.

Element (wt.%)	A	B	C	D	E
Zn	1.03	19.09	28.44	21.78	0.98
S	0.49	2.33	4.98	3.41	0.24
F	1.47	9.86	10.34	8.71	1.04
O	70.42	52.20	44.87	50.97	71.23
C	25.50	16.38	10.53	14.02	25.80
N	1.09	0.14	0.84	1.11	0.71